NASA TECHNICAL NOTE

MAGNETIC FLUX FLOW IN A TYPE II SUPERCONDUCTOR

by Eugene Willard Urban

George C. Marshall Space Flight Center
Marshall Space Flight Center, Ala. 35812

NATIONAL AERONAUTICS AND SPACE ADMINISTRATION • WASHINGTON, D. C. • MARCH 1971

1. Report No.	2. Government Accession No.	3. Recipient's Catalog No.
NASA TN D-6244		

4. Title and Subtitle	5. Report Date
MAGNETIC FLUX FLOW IN A TYPE II SUPERCONDUCTOR	March 1971
	6. Performing Organization Code
7. Author(s)	8. Performing Organization Report No.
E. W. Urban	M438
9. Performing Organization Name and Address	10. Work Unit No.
George C. Marshall Space Flight Center Marshall Space Flight Center, Alabama 35812	11. Contract or Grant No.
	13. Type of Report and Period Covered
12. Sponsoring Agency Name and Address	Technical Note
National Aeronautics and Space Administration Washington, D. C. 20546	14. Sponsoring Agency Code

15. Supplementary Notes

Prepared by Space Sciences Laboratory
Science and Engineering Directorate

16. Abstract

An experimental study has been conducted to measure the flow of magnetic flux through the wall of a specimen of Nb25%Zr, and thereby to infer the magnetic induction and currents in the material. It was found that if at some magnetic field the specimen were heated to above T_c and recooled, then if the applied field were subsequently changed at a constant rate, the rate of flux flow into or out of the sample would increase linearly with time. If measured at a series of magnetic fields, the rates of these increases, or the flow rate slopes were found to be a smoothly increasing function of average applied field. Calculations based on eight published critical current density models did not satisfactorily explain these observations. It was found, however, that the empirical current density model $J_c = \alpha_c \frac{\mu_0 H_{c2} - B}{B_0 + B}$ did, in fact, give excellent agreement with the measured flow rate behavior. In this report the experimental and analytical results are described and the new critical current density model is compared with earlier ones.

17. Key Words (Suggested by Author(s))	18. Distribution Statement
	Unclassified - Unlimited

19. Security Classif. (of this report)	20. Security Classif. (of this page)	21. No. of Pages	22. Price*
Unclassified	Unclassified	76	$3.00

*For sale by the National Technical Information Service, Springfield, Virginia 22151

TABLE OF CONTENTS

	Page
INTRODUCTION	1
BACKGROUND DISCUSSION	7
FLUX FLOW MEASUREMENTS	13
FLUX FLOW CALCULATIONS	18
STOP-HEAT FLUX FLOW MEASUREMENTS	26
COMPARISON OF CALCULATIONS AND DATA	32
NEW CRITICAL CURRENT DENSITY MODEL	37
DISCUSSION OF THE NEW MODEL	48
SUMMARY	50
APPENDIX A: EXPERIMENTAL DETAILS AND ADDITIONAL MEASUREMENTS	53
APPENDIX B: CALCULATION RESULTS — PUBLISHED MODELS	60
APPENDIX C: CALCULATION RESULTS — NEW MODEL	67
REFERENCES	69

LIST OF ILLUSTRATIONS

Figure	Title	Page
1.	Sample holder with sample.	3
2.	Experimental apparatus.	4
3.	Oscilloscope traces from a typical flux jump.	6
4.	Magnetization of Type II Superconductors.	9
5.	Magnetic field and current distributions in a hollow cylinder	10
6.	Typical flux flow voltage data; continuous field sweep mode	15
7.	Flux flow rate slopes; increasing H; continuous field sweep mode.	16
8.	Flux flow rate slopes; decreasing H; continuous field sweep mode	17
9.	Induction distribution and calculation notation	19
10.	Typical flux flow voltage data; stop-heat mode.	27
11.	Flux flow rate slopes; stop-heat mode; all sweep rates	29
12.	Flux flow rate slopes; stop-heat mode; $\dot{H} = 49$ G/s	30
13.	Flux flow rate slopes; stop-heat mode; all sweep rates	31
14.	Flux flow rate slope calculations.	33

LIST OF ILLUSTRATIONS (Concluded)

Figure	Title	Page
15.	Flux flow rate slope calculations	34
16.	Variation of Kim model α with field	38
17.	Flux flow rate slope calculation; new model	40
18.	Flux flow rate slope calculation; new model; $\dot{H} = 49$ G/s	41
19.	X-Y record of bore and applied fields; $\dot{H} = 20$ G/s	43
20.	Induction in tube wall for experiment of Figure 19; calculated from new model	44
21.	Critical current density functions with improper high field behavior	46
22.	Critical current density functions with proper high field behavior	47
A-1.	X-Y record of bore and applied fields near H_{c2}	57
A-2.	X-Y pen separation near H_{c2}	59

INTRODUCTION

The magnetic properties of Type II superconductors have been studied extensively by many researchers [1][1] and, presently, a relatively good understanding exists of the sources of hysteresis and magnetic instabilities in these materials. However, new effects continue to be observed[2] [2] and, in addition, neither theoretical nor empirical models have been found which can fully describe or explain more than limited amounts of published data [1].[3]

To contribute to a more complete understanding of the magnetic behavior of Type II superconductors, an experiment was conducted to measure the way in which magnetic flux moves into and out of a sample under the influence of a changing applied field. Based on an extensive body of published information [1][4] and on prior experience [2], we expected to obtain two types of flux motion information. First, as the external field H applied to such a sample is varied slowly, a relatively slow flow of flux through the sample

---

1. See, for example, Reference 1 and the references therein.
2. M. S. Lubell and E. W. Urban have independently observed large magnetic flux flow oscillations apparently related to the onset of instabilities.
3. See, for example, Reference 1 and the references therein.
4. Ibid.

wall occurs. This flux flow into or out of the superconductor is understood to produce spatial variations in the induction or flux density B within the material. Knowledge of flux flow characteristics would then permit inferences to be made of the distribution, motion, and causes of such flux density gradients.

Second, as H changes over a wide range, the induced gradients spontaneously collapse at more or less regular field intervals, producing very rapid flux motion. During these flux jumps, as they are called, redistribution of flux occurs throughout much or all of the sample volume. Knowledge of the velocity of the jumps and conditions for jump initiation would give information concerning the thermal and magnetic diffusion properties of the superconductor, and the occurrence of macroscopic flux instabilities.

The work reported here concerns a series of flux flow measurements and the conclusions drawn from them. A schematic of the sample and sample holder arrangement used for the measurements is shown in Figure 1 and an overall schematic of the measurement instrumentation is given in Figure 2. A hollow cylindrical sample of Nb25%Zr with outer radius a and inner radius b was placed coaxially in the bore and at the midplane of a superconducting solenoid which provided the applied field H and permitted H to be swept at controlled rates or held constant. Hall effect probes near the sample midplane at the outer wall and in the sample bore directly measured H and the bore field H' respectively, following a technique used first by Kim and coworkers [3].

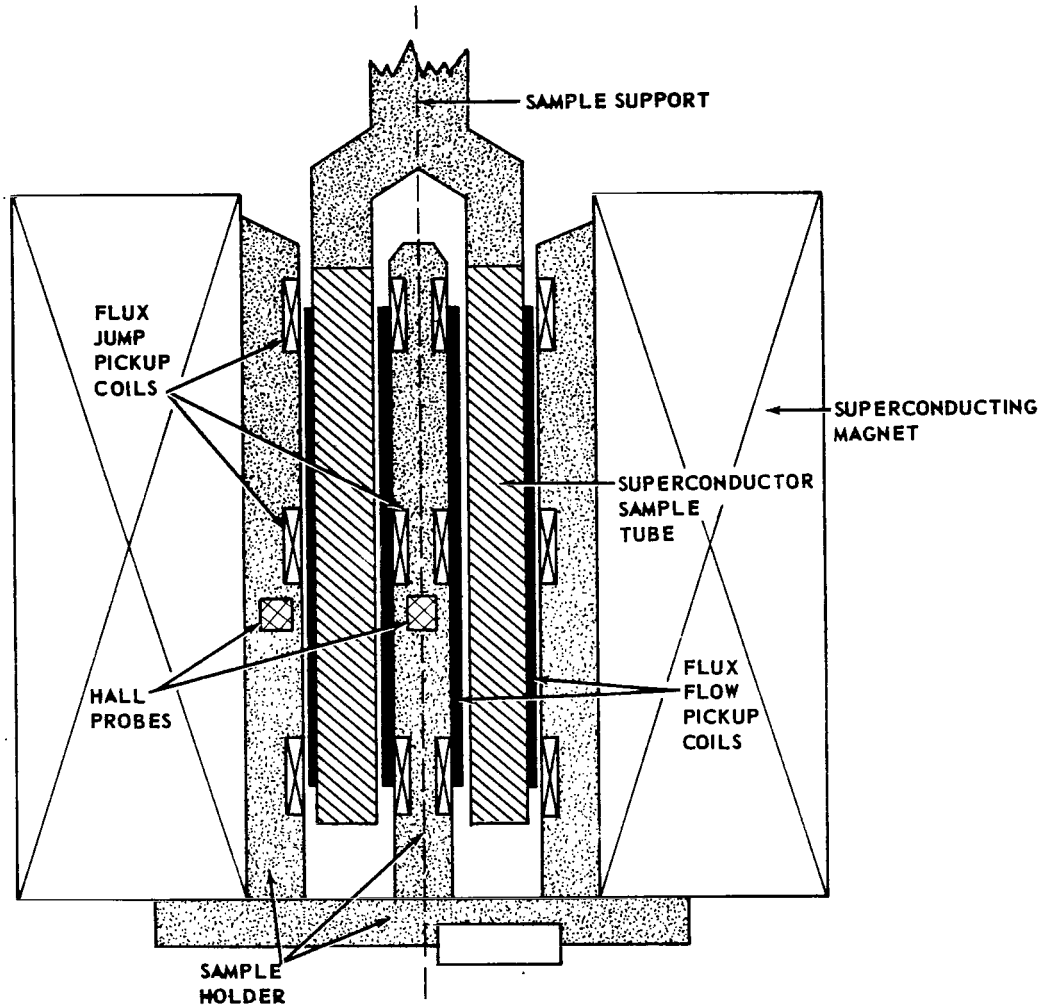

Figure 1. Sample holder with sample.

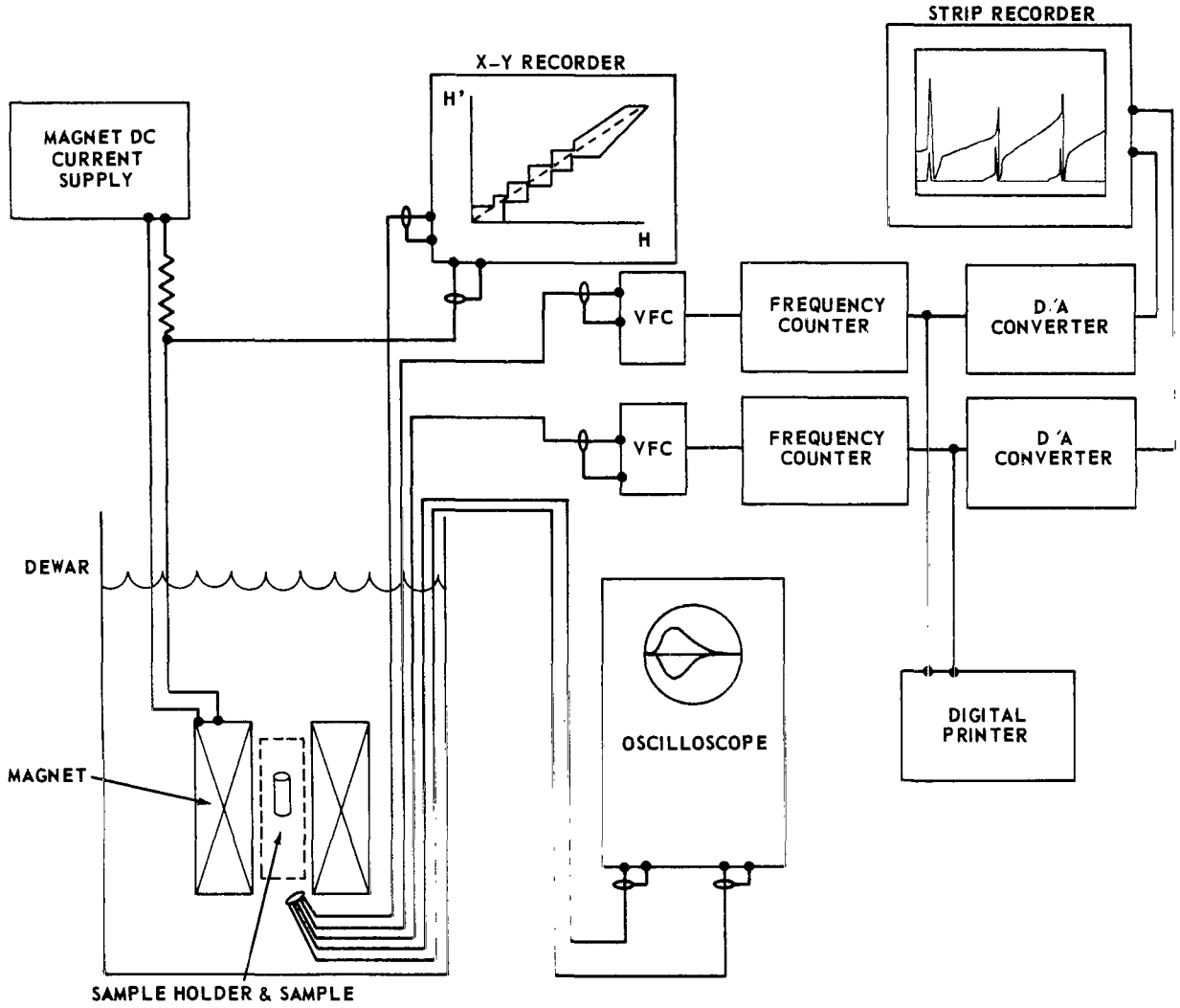

Figure 2. Experimental apparatus.

The rates of flux flow through the specimen walls, which we call $\dot{\phi} = \frac{d\phi}{dt}$, were measured by windings covering approximately three-fourths of the sample length. The single layer outer coil was wound directly on the specimen, while the multilayer inner coil was wound on a plastic insert shaft which also carried the inner Hall probe and three flux jump pickup coils. Descriptions of the high gain integrating digital voltmeters for measuring $\dot{\phi}$ and $\ddot{\phi}$ and of other measurements are given in Appendix A. Flux flow voltages typically ranged from a few to a few hundred microvolts, depending primarily on the field sweep rate $\dot{H}$.

Six flux jump pickup coils provided radial and axial flux jump motion information. Three identical coils were mounted near the outer wall, one at the midplane and one at each end; the other set of three coils referred to earlier were similarly placed in the tube bore. The six jump signals, typically a few volts maximum amplitude and a few milliseconds duration, were displayed simultaneously on an oscilloscope and photographed. A representative set of pulses for a flux jump is shown in Figure 3. It can be seen that the jump started near the bottom of the sample at the outside and proceeded upward and inward.

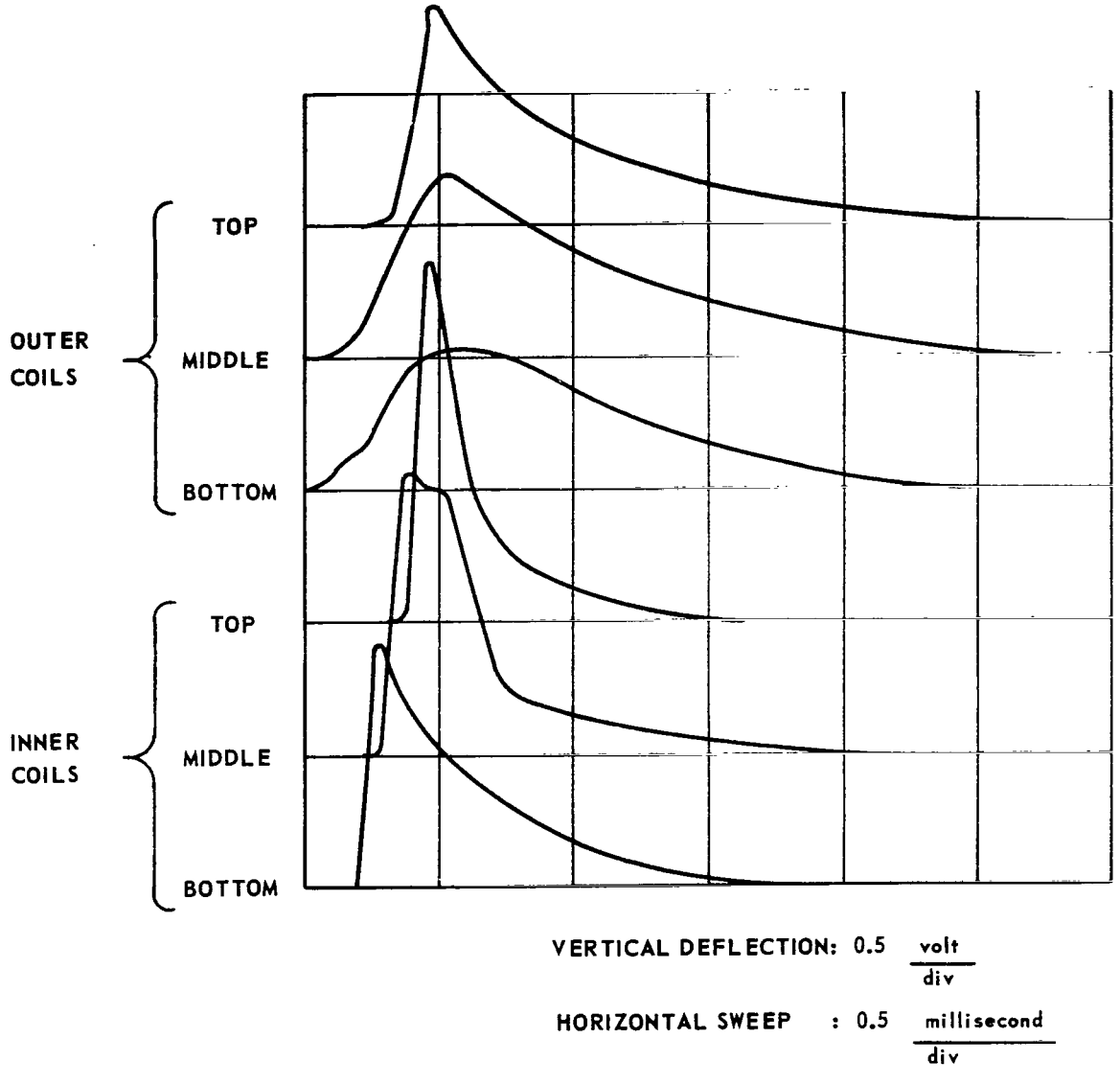

Figure 3. Oscilloscope traces from a typical flux jump.

BACKGROUND DISCUSSION

To provide a clearer understanding of the measurements to be described, a brief summary of the present understanding of the general magnetic properties of Type II materials is in order. Although all superconductors are diamagnetic and strongly oppose the entry of magnetic flux into their interiors, Type II superconductors permit limited flux penetration in the form of flux quanta or fluxoids. The fluxoids can be visualized [4] as filamentary current vortices with small, normal phase cores which carry most of the field. The amount of flux in one fluxoid is $\phi_0 = \frac{h}{2e} = 2.07 \times 10^{-15}$ weber, where h and e are Planck's constant and the electronic charge, respectively. The field in a fluxoid decreases very rapidly with radial distance into the superconducting phase outside of the core, with the result that even at relatively high fields where fluxoids are densely packed, an appreciable portion of the volume of the material is superconducting and is available to carry nondissipative currents.

If a sample of so-called <u>ideal</u> Type II material is placed in a slowly increasing field H, the following is understood to occur. At fields less than a lower critical field H_{c1}, flux cannot enter the specimen because of the Meissner effect, a condition of perfect bulk diamagnetism. Above H_{c1},

fluxoids nucleate at the sample boundary and move freely into the interior. Mutual fluxoid repulsion leads to a regular distribution of vortices throughout the ideal sample, their area density being the induction $\vec{B}$. $\vec{H}$ is related to $\vec{B}$ by

$$\vec{H} = \frac{1}{\mu_0} \vec{B} - \vec{M} , \qquad (1)$$

where $\vec{M}$ is the magnetic moment due to the spontaneous diamagnetic currents which flow at the specimen surface. A plot of $-\vec{M}$ versus $\vec{H}$ for this situation is shown in Figure 4a.

As H increases further, more of the specimen volume is occupied by normal fluxoid cores and $-\vec{M}$ decreases. Above the upper critical field H_{c2}, the sample bulk is completely normal, and the magnetization is zero. Since flux flow is unrestricted, the curve of Figure 4a is reversible; an ideal Type II superconductor is not hysteretic. When $H_{c1} < H < H_{c2}$, the superconductor is said to be in the mixed state.

In a real, disordered Type II material, such as the NbZr alloy used in this study, fluxoid motion is strongly inhibited by a process known as pinning [1]. Pinning centers have been identified as defects, dislocations, voids, precipitate particles, and many other types of microstructural features which are nearly unavoidable in technical materials. An important result of pinning is the existence of magnetic hysteresis, indicated in Figure 4b for three hypothetical materials. Pinning also leads to rapid spatial variations in flux density in such materials, as shown schematically on the right side of Figure 5

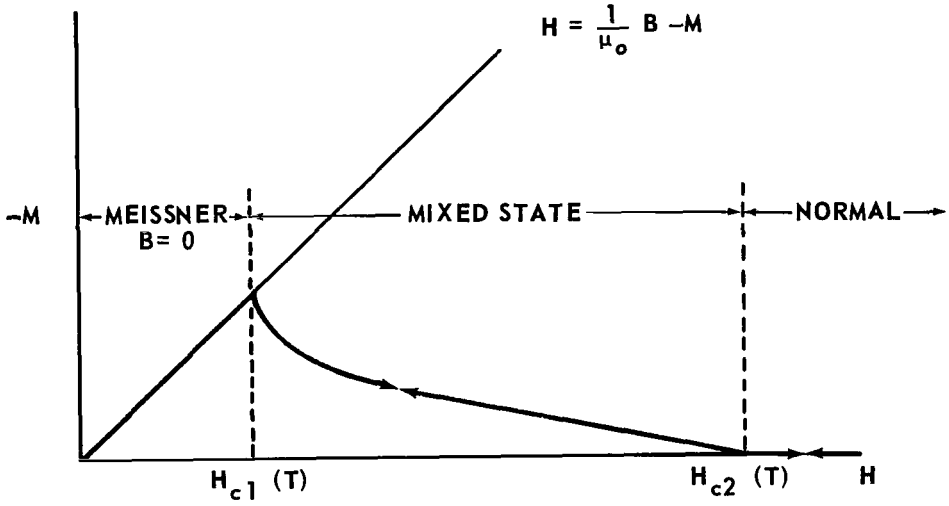

(a) IDEAL TYPE II

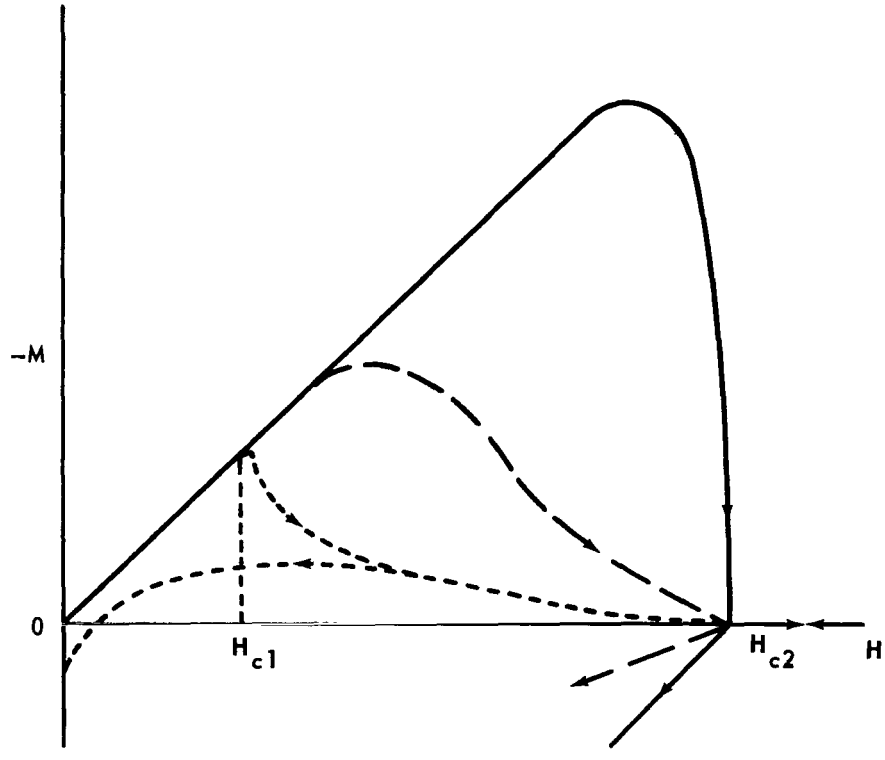

(b) DISORDERED TYPE II

Figure 4. Magnetization of Type II Superconductors.

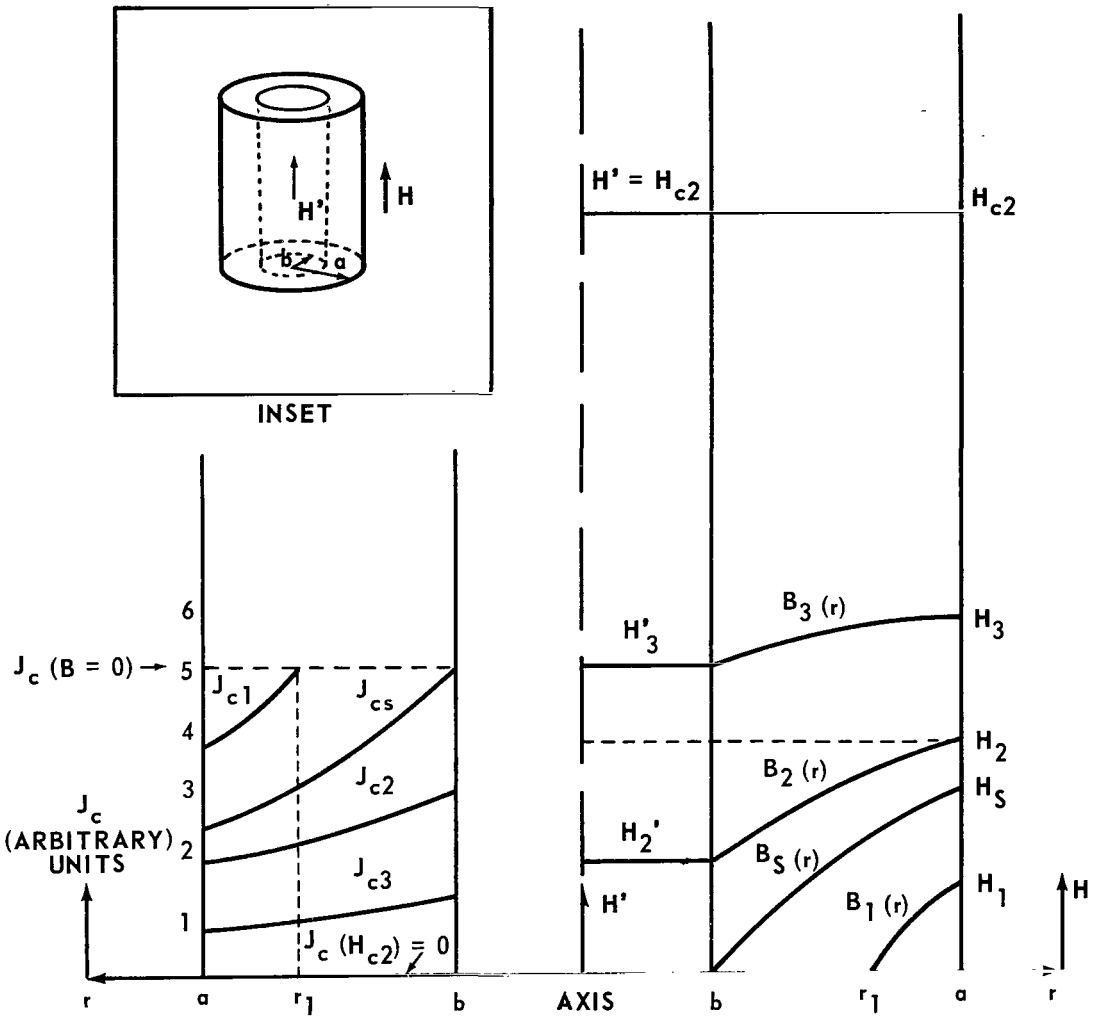

Figure 5. Magnetic field and current distributions in a hollow cylinder.

for the cylindrical specimen arrangement indicated in the inset. If, for example, the applied field has increased from zero to H_1, B varies in some manner from $\mu_0 H_1$ at $r = a$ to zero at $r = r_1$. Further increase of H can produce the succeeding induction distributions shown.

Consider the Maxwell equation

$$\nabla \times \vec{H} - \dot{\vec{D}} = \vec{J} \quad . \tag{2}$$

For very slowly changing fields, $\vec{D}$ and $\dot{\vec{D}}$ can be neglected. In our cylindrical geometry, equation (2) then reduces to the scalar form

$$\frac{dB}{dr} = -\mu_0 J \quad , \tag{3}$$

where J is a diamagnetic, azimuthal current density. Thus the local flux density gradient $\frac{dB}{dr}$ is proportional to the local current density, and both vary with B. For example, when the applied field is H_1, $J_{c1}(B)$, defined below, flows in the layer $r_1 < r < a$, as indicated in the left side of Figure 5. Two arguments demonstrate that as flux tries to overcome the pinning forces, it tends to move down the induction gradients. First, mutual fluxoid repulsion insures that motion will be toward regions of reduced flux density. Second, the Lorentz force $F_L = JB = -\frac{1}{\mu_0} B \frac{dB}{dr}$ existing between the local current density and the individual fluxoids comprising B can be seen to be in the direction of decreasing B. If one calls the net local pinning force at a point in the superconductor F_P, then one may argue intuitively that flux will be almost completely pinned until F_L just exceeds F_P [5]. One can define a critical pinning condition as existing when

$$F_L = F_P \quad . \tag{4}$$

In this situation, maximum induction gradients exist and $J(B)$ is called the critical current density $J_c(B)$. Then the magnitude of the Lorentz force is $J_c B$ and, if the functional behavior of F_P can be specified or inferred for a material, then the functional behavior of $J_c(B)$ can be calculated, with the aid of equation (4).

On the basis of these last arguments, flux flow can be understood as the slow process of flux entry into or departure from a sample to establish the internal flux distributions, which are, in turn, governed by the critical current density function. Similarly, flux jumps result when the critical flux density gradients collapse. This leads to rapid redistribution of flux and to dissipation of the critical currents. For example, if a complete flux jump were to occur at $H = H_2$ of Figure 5, then at the conclusion of the jump, the field distribution would be as indicated by the dotted line, and J_c would have vanished. Frequently in flux jump experiments it is found that the currents do not fully dissipate. Following such incomplete jumps, local regions of inhomogeneous flux distribution exist, together with the circulating currents which maintain them.

FLUX FLOW MEASUREMENTS

Consider a flux flow measurement which starts from a condition of constant induction B_j throughout the sample wall. The applied and bore fields are H_j and H'_j, respectively, and $H_j = \frac{1}{\mu_0} B_j = H'_j$. Based on the work of Coffey [6] and of Wipf and Lubell [7], it was anticipated that this uniform field condition would be, in fact, well satisfied at the conclusion of most flux jumps because of the complete dissipation of the currents. As H is then increased or decreased by a small increment, a small amount of flux will enter or leave a thin annular region at the outer wall with some measured flow velocities $\pm\dot{\phi}_1$, respectively. If H continues to change at the same rate, then during the next instant flux must enter or leave a thicker annular layer and must fill or deplete the layer to a greater average induction increment than in the preceding moment. Therefore, the magnitude of the new measured flow rate $\pm\dot{\phi}_2$ will be greater than that of $\pm\dot{\phi}_1$. Qualitatively, $\dot{\phi}$ will increase smoothly in magnitude with H, if the field sweep rate $\dot{H}$ is constant. The sign of $\dot{\phi}$ will be that of $\dot{H}$, positive for increasing field and negative for decreasing field. The quantitative behavior of $\dot{\phi}$ will depend on the exact nature of J(B) through equation (3) and its integrals.

A typical flux flow voltage variation measured for the NbZr sample with continuous, constant field sweep rate is shown in Figure 6. Flux flow voltage was recorded versus time, or equivalently versus H, since $\dot{H}$ was constant. Immediately after each flux jump, which appeared as a large voltage pulse,[5] the flux flow voltage dropped to a small value, increased rapidly, then rose linearly and much more slowly. There was no observable change in the form of the flux flow voltage, if the field sweep was stopped after each jump to insure that the sample was fully cooled to the helium bath temperature.

The combination of the rapid flow voltage rise, followed by the slower increase, was not immediately understandable. A qualitative explanation of this behavior was proposed later and is described below. The interesting linear regions, each representing a constant flux flow rate increase $\ddot{\phi}$, were found to vary systematically with field. In Figures 7 and 8 the slopes of these linear intervals are plotted as a function of the applied field at the midpoint of each interval for several values of $\dot{H}$. Figure 7 shows $\ddot{\phi}$ for increasing H. The flux flow slopes have a maximum at about 6 kilogauss, dip through a flat minimum, then rise smoothly. For decreasing H (Fig. 8), no peak appears.

---

5. Note that this integrated pulse is simultaneous with, but obscures the details of, the type of pulse data shown in Figure 3.

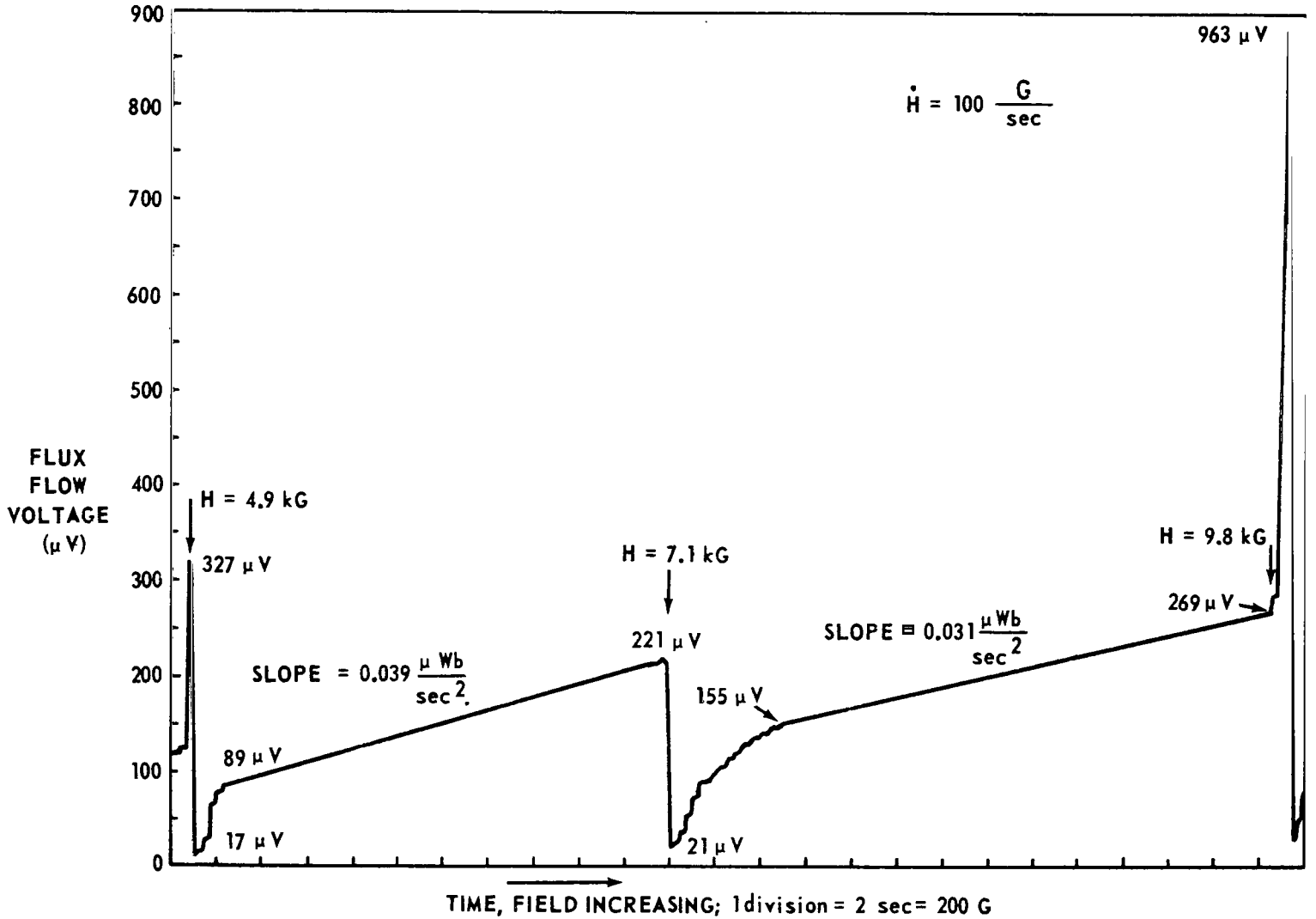

Figure 6. Typical flux flow voltage data; continuous field sweep mode.

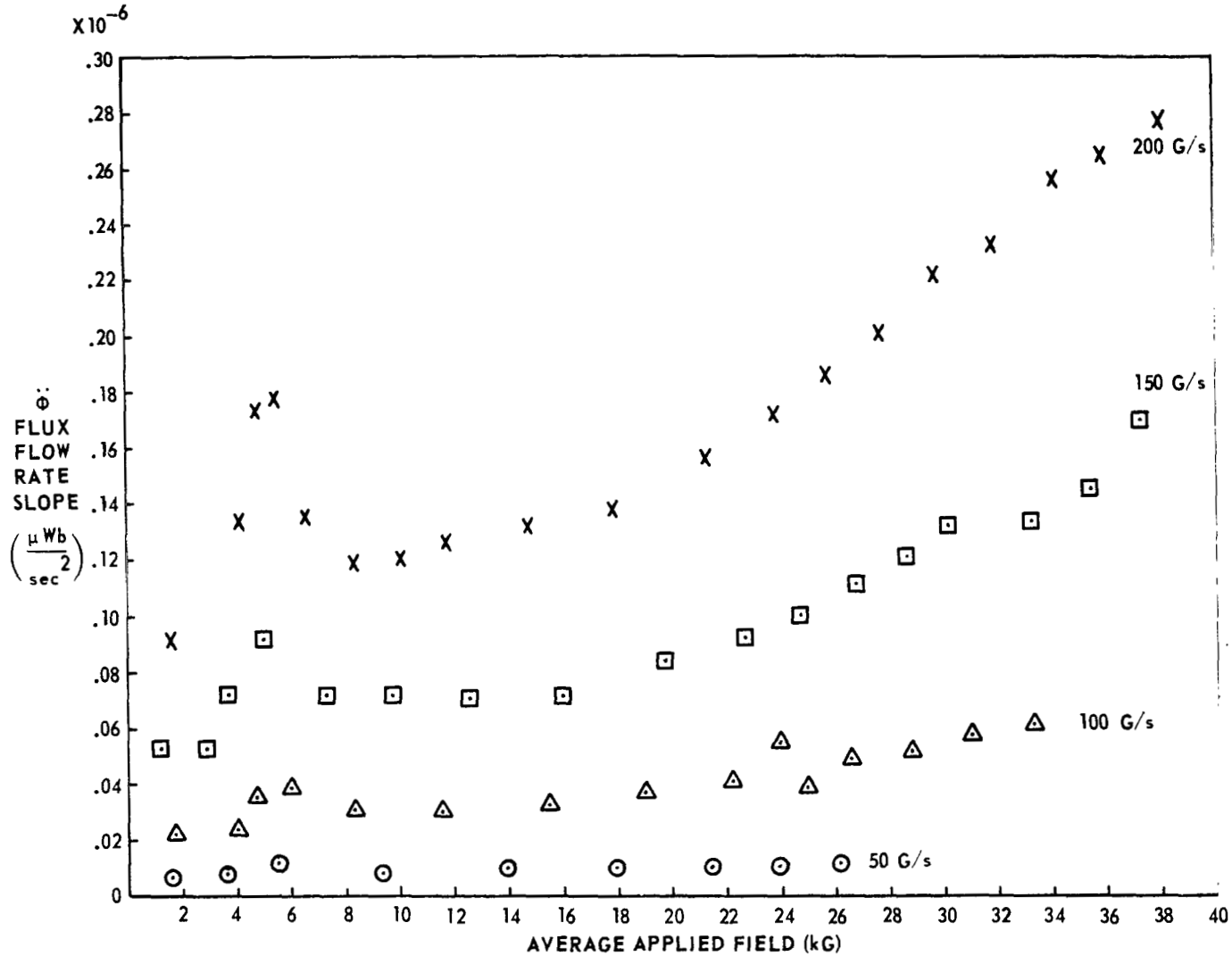

Figure 7. Flux flow rate slopes; increasing H; continuous field sweep mode.

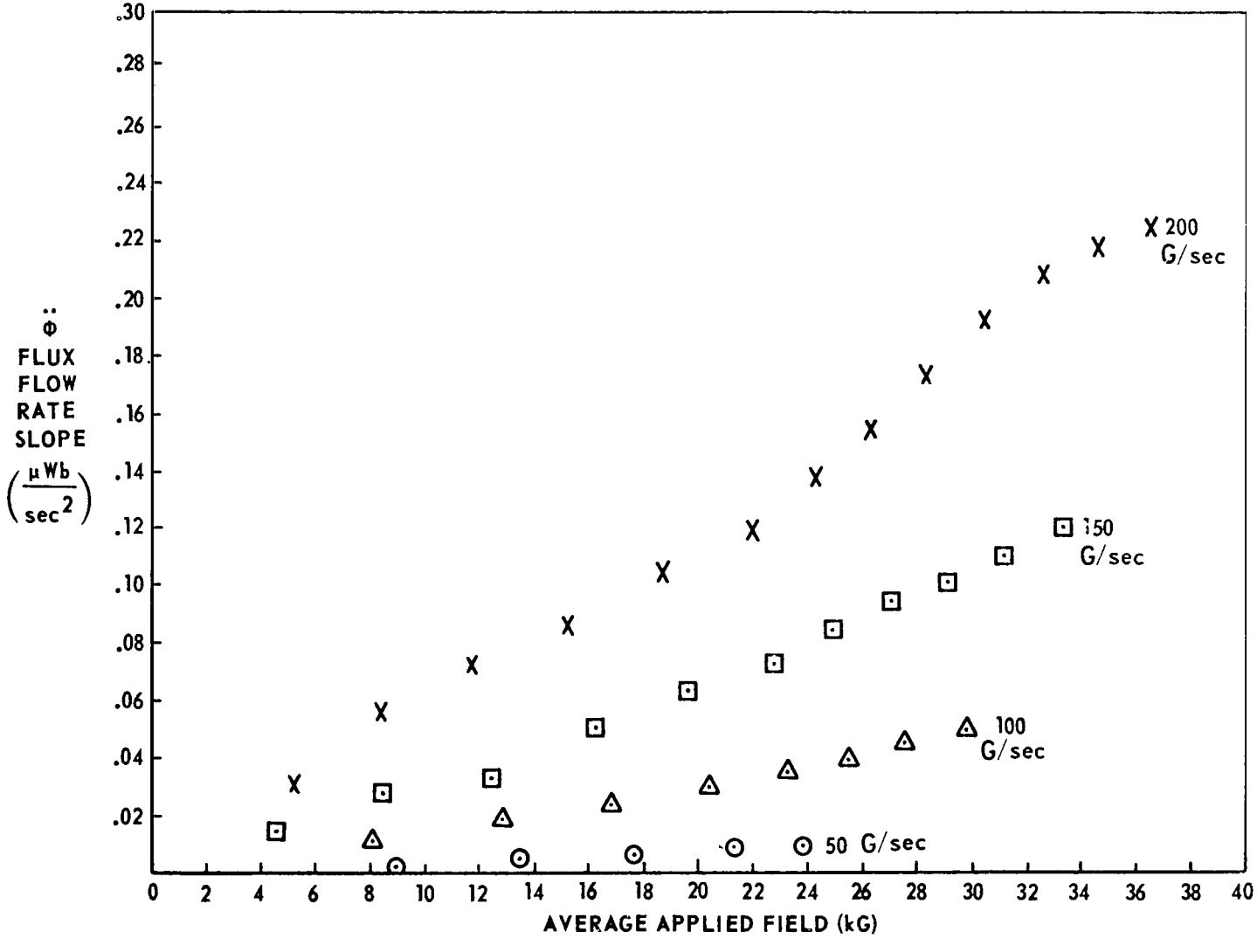

Figure 8. Flux flow rate slopes; decreasing H; continuous field sweep mode.

FLUX FLOW CALCULATIONS

Following the observation of these regular flux flow rate features, we sought to verify them analytically. A calculation was made of the flux distributions and flux flows to be expected in a cylindrical specimen. It was assumed that each smooth flux flow sequence would start from a uniform field condition $B_j = \mu_0 H_j$, as in Figure 9. It was further assumed that when H had changed by some amount H_a (less than that required to cause the next jump), one of the two quasistatic situations shown schematically in Figure 9 would apply with

$$H = H_j \pm H_a \quad , \tag{5}$$

the upper and lower signs referring to $\dot{H} > 0$ and $\dot{H} < 0$, respectively. r_{min} is the radial distance to which the change in $B(r)$ has penetrated; it depends on H_j and H_a, and on the particular $J_c(B)$.

In order to guarantee that the induction distribution $B(r)$ was indeed quasistatic, one had to assume that the processes of thermally activated flux creep, described originally by Anderson [8] and Kim et al. [3,9], could be neglected. Thus if the field sweep were stopped at any level, the $B(r)$ at

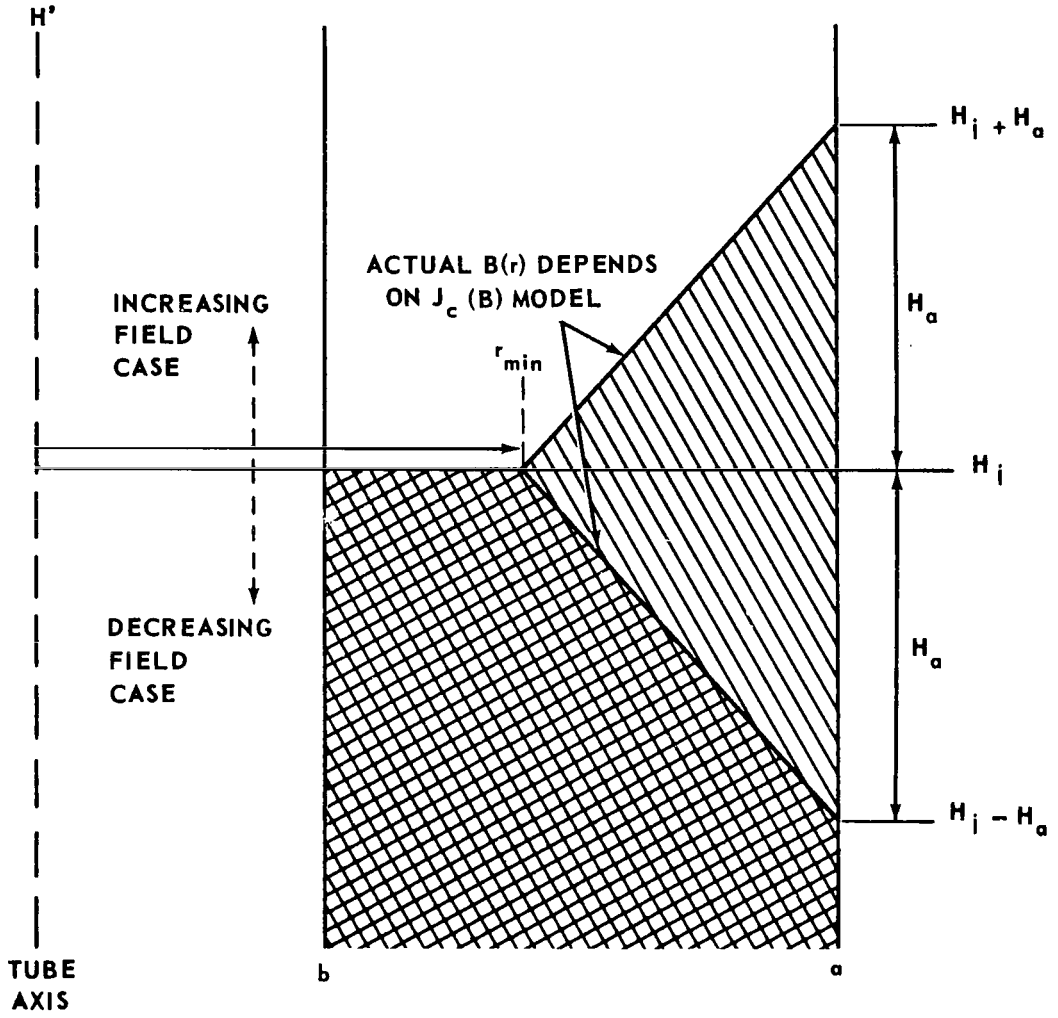

Figure 9. Induction distribution and calculation notation.

that instant would cease changing, and $\dot{\phi}$ should very quickly become zero. Restart of the sweep at the same rate should then cause $\dot{\phi}$ to return immediately to the same amplitude and slope which existed when the sweep was stopped. On the other hand, the occurrence of appreciable flux creep after the sweep was stopped would cause a gradual $\dot{\phi}$ decrease to zero and would allow $B(r)$ to change somewhat, giving rise to a different amplitude and slope upon sweep restart. During the series of experiments, it was verified several times that a sweep stop, followed by several seconds wait, then sweep restart did, in fact, give the behavior expected for a quasistatic situation in which flux creep was negligible.

To indicate the complete functional dependencies of our problem, we rewrote equation (3) in the form

$$\frac{dB(r,t)}{dr} = -\mu_0 J_c \left[B(r,t)\right] \quad . \tag{6}$$

It remained only to specify a functional behavior of J_c and to integrate equation (6) to obtain the variation of induction with radial position in the specimen. The boundary conditions are $B(a) = \mu_0 (H_j \pm H_a)$ and $B(r_{min}) = \mu_0 H_j$.

Currently eight essentially different models for the field dependence of critical current density of Type II superconductors have been proposed in the literature. They are summarized in Table 1, with references to the works in which they appear. In each model, α is assumed to be a

TABLE 1. CRITICAL CURRENT DENSITY MODELS

Model	J_c	References
Bean-London (BL)	α	10, 11
Kim (K)	$\frac{\alpha}{B_0 + B}$	12
Anderson-Friedel-Silcox (AFS)	$\frac{\alpha}{B}$	8, 13, 14
Yasukochi (Y)	$\frac{\alpha}{B^{1/2}}$	15
Irie (I)	$\frac{\alpha}{B^{\gamma-1}}$	16
Fietz (F)	$\alpha \exp\left(-\frac{B}{\beta}\right) + \gamma$	17
Goedemoed (G)	$\alpha(\mu_0 H_{c2} - B)$	18
Alden-Campbell-Coffey (ACC)	$\alpha \frac{\mu_0 H_{c2} - B}{B^{1/2}}$	19, 20, 21

temperature dependent constant.[6] For the Kim model, B_0 is a constant whose physical meaning is not clear. Empirically it has been found that B_0

6. For the following reason, temperature effects were not considered in the calculations. Experimentally, the sample was fairly completely exposed to the liquid helium bath, so that if the thermal conductivity of the superconductor were large enough and the rate of heat generation due to dissipative flux motion were small enough, a constant sample temperature equal to the bath temperature 4.2°K could be expected. Wipf and Lubell [7] state that for a Nb25%Zr sample approximately of the present specimen size, a uniform, constant temperature condition will exist throughout, so long as $\dot{H}$ is less than about 10^4G/s . Since maximum $\dot{H}$ was 200 G/s , the isothermal assumption was justified.

is of the order of a few kilogauss for NbZr and NbTi alloys and Nb_3Sn. For the Irie model, γ is a number which should lie in the range $1 \leq \gamma \leq 2$.

Having obtained from the integration of equation (6) an expression for $B(r,t)$ or, as is the case for some of the models, an expression for $r(B,t)$, the instantaneous total flux $\phi(t)$ in the sample can be calculated. Since induction B is flux density or flux per unit area, the total flux in the specimen wall is given by an integral of B over the area of the cylinder cross section,

$$\phi(t) = 2\pi \int_0^a B(r,t)\, r\,dr$$

$$= 2\pi \int_0^{r_{min}} \mu_0 H_j\, r\,dr + 2\pi \int_{r_{min}}^a B(r,t)\, r\,dr \quad . \tag{7}$$

$$\phi(t) = \pi \mu_0 H_j r_{min}^2 + 2\pi \int_{r_{min}}^a B(r,t)\, r\,dr \quad . \tag{8}$$

The first term in equation (8) represents the total flux within the cylindrical region $0 < r \leq r_{min}$ due to the field H_j of the previous jump. Since r_{min} decreases with increasing H_a, this term is a function of time. The second term is the total flux in the annular region $r_{min} < r \leq a$ in which the induction has changed from H_j.

If the specimen is a solid cylinder and $b = 0$, equation (8) is valid only if $r_{min}(H_a) > 0$. For greater H_a, flux reaches the axis from all sides and a reduced flux flow rate is required to establish a given induction on the axis.

If the specimen is hollow, equation (8) is valid only if $r_{min} \geq b$. For greater H_a, flux must flow into and across the sample wall at an increased rate to permit the bore field to increase smoothly.

Our primary concern in these calculations was the determination of $\dot{\phi}(t)$ and $\ddot{\phi}(t)$. It would, therefore, have been possible to avoid a major calculation step by differentiating equation (8) directly. However, since the total flux in the sample as a function of field could be found from the experiments simply by measuring the area under the flux flow rate curves, an explicit expression for $\phi(t)$ was considered valuable. Consequently, except for the Fietz (F) model, $\phi(t)$ was determined. It is clear that

$$\dot{\phi}(t) = \frac{\partial \phi}{\partial H} \frac{dH}{dt} = \frac{\partial \phi}{\partial H} \dot{H} \quad , \tag{9}$$

and that

$$\ddot{\phi}(t) = \frac{\partial \dot{\phi}}{\partial H} \frac{dH}{dt} + \frac{\partial \dot{\phi}}{\partial t} \quad . \tag{10}$$

However it is assumed that $\dot{H}$ is constant so that $\frac{\partial \dot{\phi}}{\partial t} = \frac{\partial \phi}{\partial H} \ddot{H}$ vanishes. By means of equation (9), it is seen that equation (10) reduces to

$$\ddot{\phi}(t) = \frac{\partial^2 \phi}{\partial H^2} \dot{H}^2 \quad . \tag{11}$$

In our calculations we defined the following parameters:

H_j — uniform field in the sample after each jump, units are $\left(\frac{1}{\mu_0} \text{ kG}\right)$

$H_a(t)$ — applied field change from H_j $\left(\frac{1}{\mu_0} \text{ kG}\right)$

$H(t) = H_j \pm H_a(t)$	total applied field $\left(\frac{1}{\mu_0}\ \text{kG}\right)$
$\dot{H} = \pm \dot{H}_a$	rate (and direction) of applied field sweep $\left(\frac{1}{\mu_0}\ \frac{\text{G}}{\text{s}}\right)$
$B(r,t)$	flux density or induction in specimen (kG)
$\alpha = \mp \alpha_c$	proportionality constant (dimensions given for each model)
$\phi(t)$	total flux in specimen (weber, Wb)
$\dot{\phi}(t)$	rate of change of flux or flux flow rate (Wb/s)
$\ddot{\phi}(t)$	flux flow acceleration or flux flow rate slope (Wb/s^2)
$x = \frac{H}{H_{c2}} = \frac{H_j \pm H_a}{H_{c2}}$	dimensionless applied field
$x_j = \frac{H_j}{H_{c2}}$	dimensionless jump field
$\beta = \frac{B}{\mu_0 H_{c2}}$	dimensionless induction
a	sample outer radius (meter)
r_{min}	minimum radius at which B has changed (meter).

The upper and lower signs in H and $\dot{H}$ account for the increase or decrease in field for positive and negative field sweeps, while the signs in α similarly account for the diamagnetic nature of the superconducting currents. In the tables, J_c, r_{min}, $B(r,t)$ or $r(B,t)$, $\phi(t)$, $\dot{\phi}(t)$, and

$\ddot{\phi}(t)$ are shown. It should be understood that $r_{min} = r_{min}(t)$ through the time dependence of H_a, and that the three flux functions depend on H_j and H_a, as well as time.

In Appendix B are listed the results of the flux flow calculations based on the eight critical current density models of Table 1. In each expression for $\phi(t)$ the first term is seen to be the total flux contained within the outer wall due to H_j; for each interjump interval this term is independent of time.

Although calculated flux flow rates will not be shown explicitly here, it may be stated that the $\dot{\phi}$ results of all of the eight models predict a smooth rise of the flux flow rate from zero following each flux jump. There is no suggestion that the sharp breaks in the curves of Figure 5 should have been observed. This clear contradiction between the calculations and the measured flow rates led one to question the assumptions made in the calculation. Wipf suggested that the problem might stem from the acceptance of a condition of field uniformity in the sample following each jump. If, in fact, large inhomogeneities remained, then the flux would not necessarily enter smoothly nor assume a well-behaved distribution.

STOP-HEAT FLUX FLOW MEASUREMENTS

Since it was not realistic to try to modify the calculations to account for some unknown flux distributions, the experiment was modified to insure that the constant induction assumed to exist at the start of each interjump region would indeed exist. A single layer, nichrome wire heater was wound noninductively over the outer flux pickup coil and on the central pickup coil shaft. It was then possible to heat the entire specimen to above its transition temperature at each jump field to permit the field throughout the wall to become uniform and equal to the applied field H_j.

The measurements were then made in the following manner. Immediately after each jump the field sweep was stopped. The sample was then heated for approximately 5 seconds at a heater power of approximately 10 watts, which was sufficient to allow the flux to reach a quiescent, redistributed condition. Finally, the specimen was allowed to cool for 10 seconds to insure that its temperature had returned to 4.2°K, then the field sweep was restarted. Typical data for this stop-heat mode of operation over one interjump interval are shown in Figure 10. There is a smooth rise of the flow rate

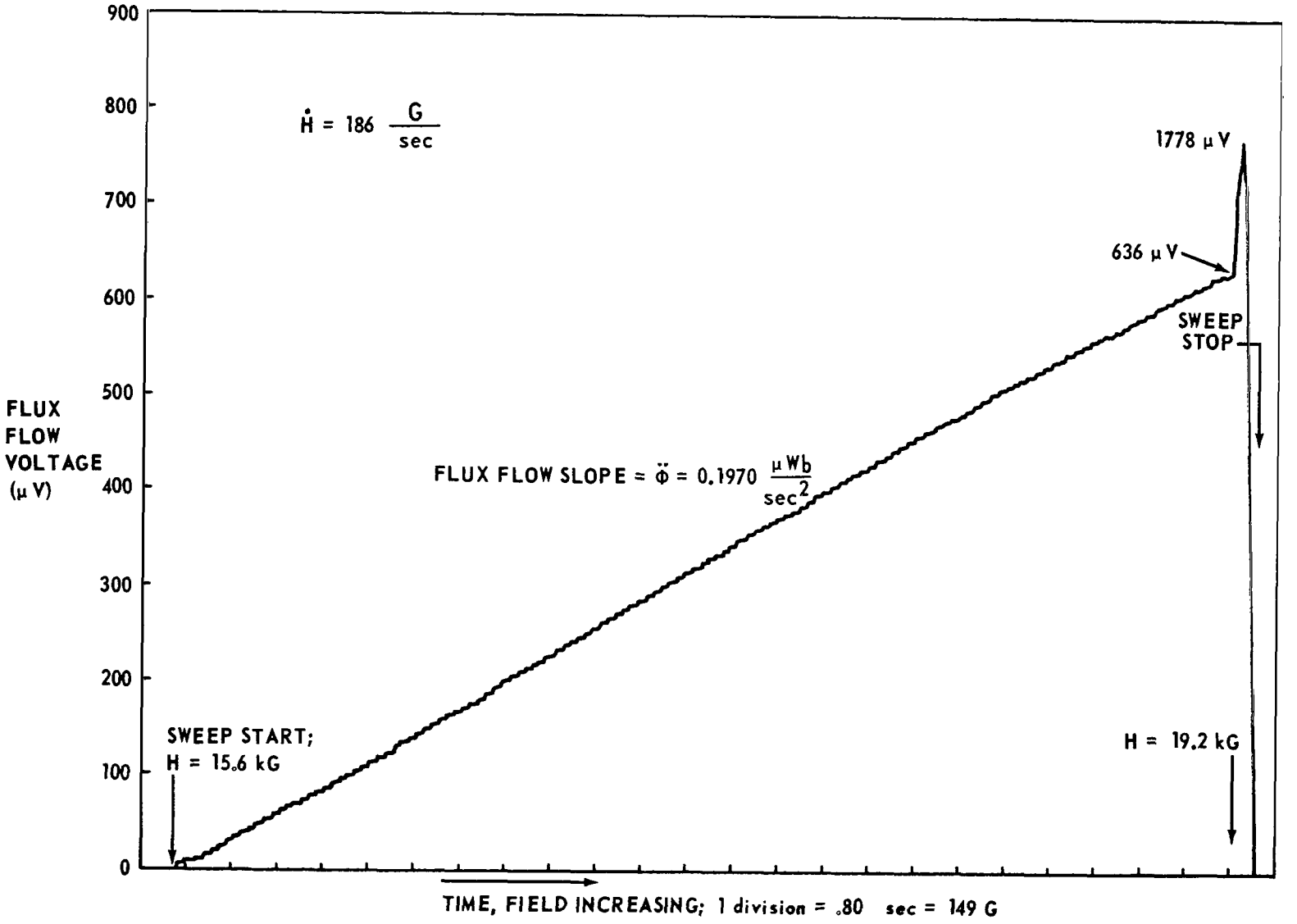

Figure 10. Typical flux flow voltage data; stop-heat mode.

from zero as predicted by the calculations. The flow rate slope $\dot{\phi}$ is approximately constant.[7] These results confirm the supposition made in the preceding section that, following each jump, the unheated specimen contains induction inhomogeneities.

Figures 11, 12, and 13 show flux flow rate slope data for the stop-heat measurements. The average slope in weber/sec^2 of each approximately linear-jump flow voltage curve is plotted versus H_a, the applied field at the midpoint of the interval. Figure 11 shows the discrete data for three sweep rates and both sweep directions. Figure 12 gives the $\dot{H} = 49$ G/s points of Figure 11 on an expanded scale. Figure 13 is a semilogarithmic plot in which curves summarize the data of Figure 11. The slopes are represented by a smoothly increasing function of average applied field (the low field peaks of Figure 7 do not occur).

7. At fields above 15kG (approximately), the data have a moderate downward curvature; in all cases the flow rate slopes are taken from linear interpolations between the endpoints of the smooth regions.

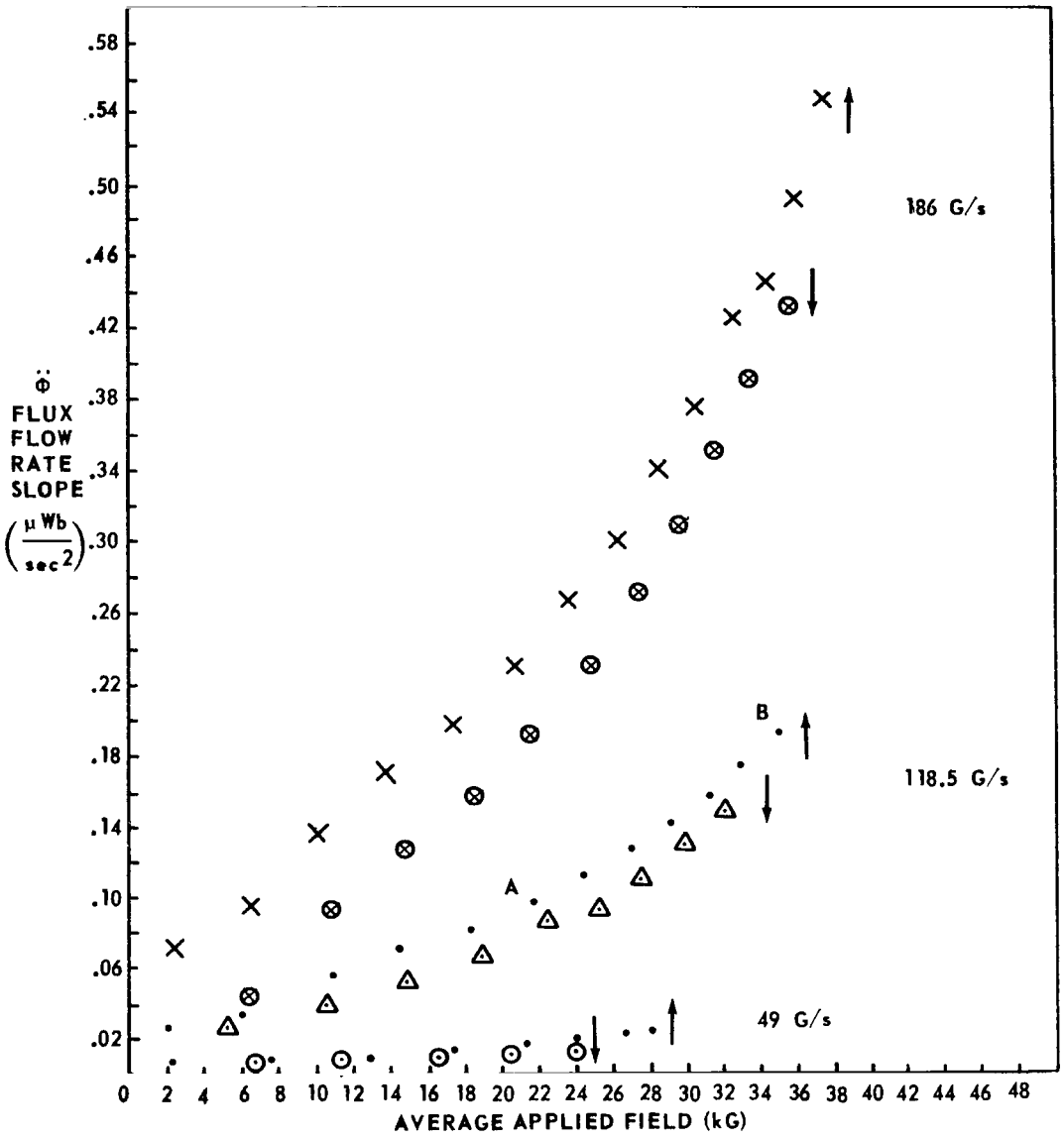

Figure 11. Flux flow rate slopes; stop-heat mode; all sweep rates.

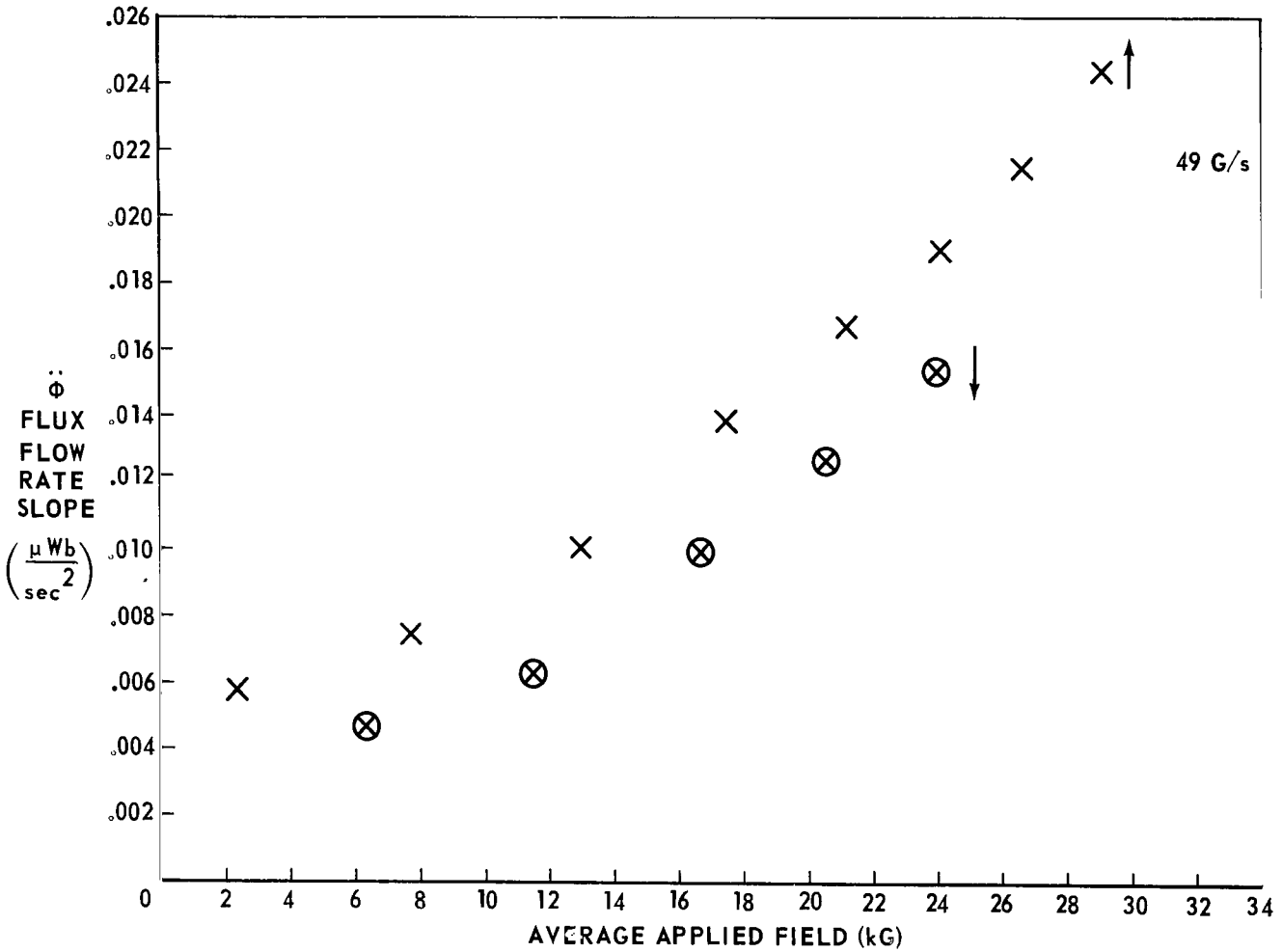

Figure 12. Flux flow rate slopes; stop-heat mode; $\dot{H} = 49$ G/s.

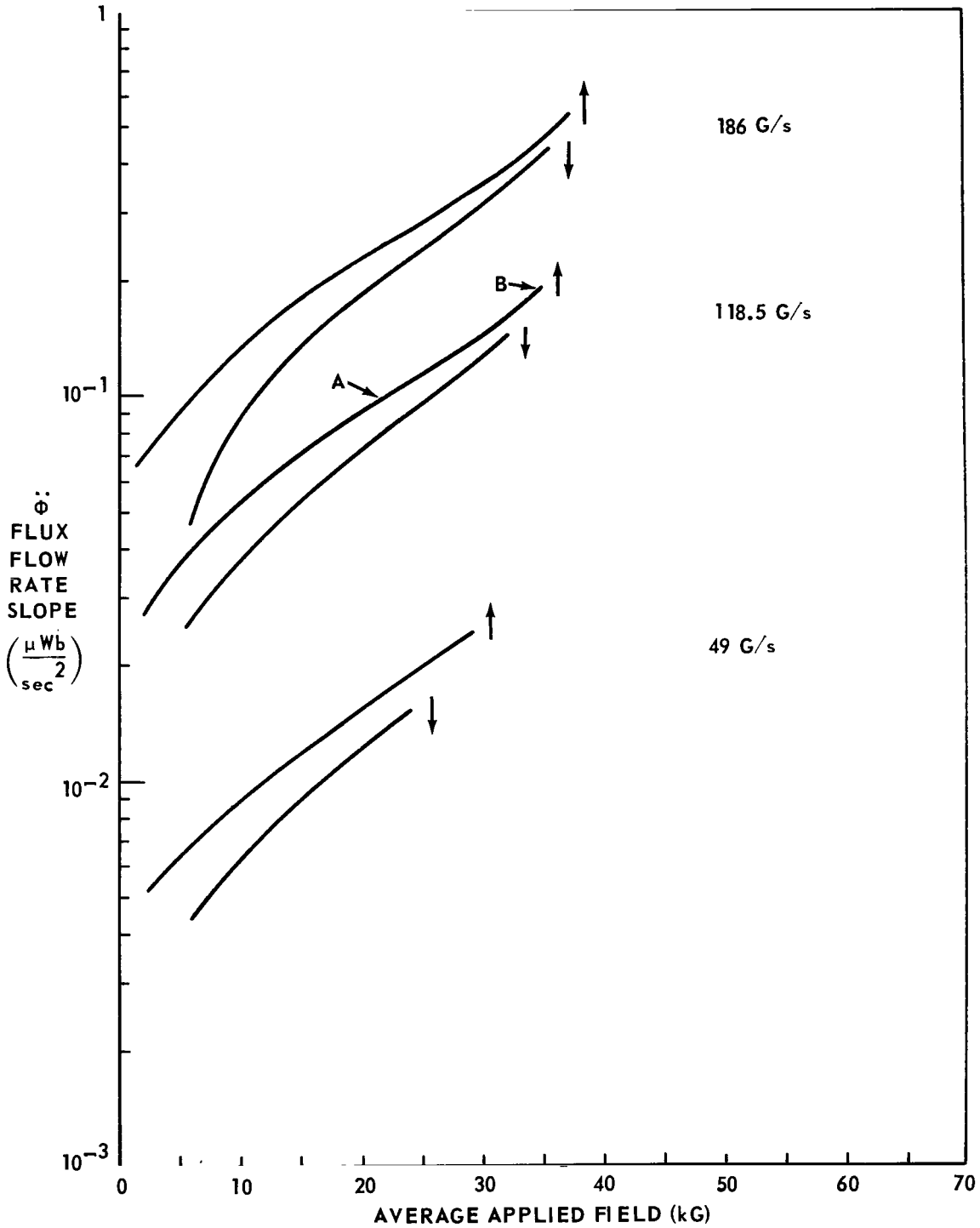

Figure 13. Flux flow rate slopes; stop-heat mode; all sweep rates.

COMPARISON OF CALCULATIONS AND DATA

In order to compare the $\ddot{\phi}$ formulas of Appendix B for the several critical current density models with the experimental results, the following procedure was used. Actual experimentally measured fields were used in solving the $\ddot{\phi}$ equations: H_j was taken to be the applied field observed following each heating and recooling; H_a was one-half of the subsequent constant slope interjump interval. Thus $H = H_j \pm H_a$ was the midpoint field of each interjump region. The constant α was chosen for each model so that the calculation fit the $\dot{H} = 118.5$ G/s curve at point A of Figure 12. This fit point was chosen, since it applies to an intermediate field, where presumably all of the models should be reasonably applicable, and it applies to an intermediate value of $\dot{H}$. For point A the parameters have the following experimental values: $\ddot{\phi} = 0.0971$ Wb/s^2; $\dot{H} = 118.5$ G/s; $H_j = 20.10$ kG; $H_a = 1.53$ kG; $H = 21.63$ kG.

The results of the $\ddot{\phi}$ calculations are shown in Figures 14 and 15. The same 118.5 G/s data have been replotted three times in each figure to separate the various curves for clarity. Curves for three values of B_0 for

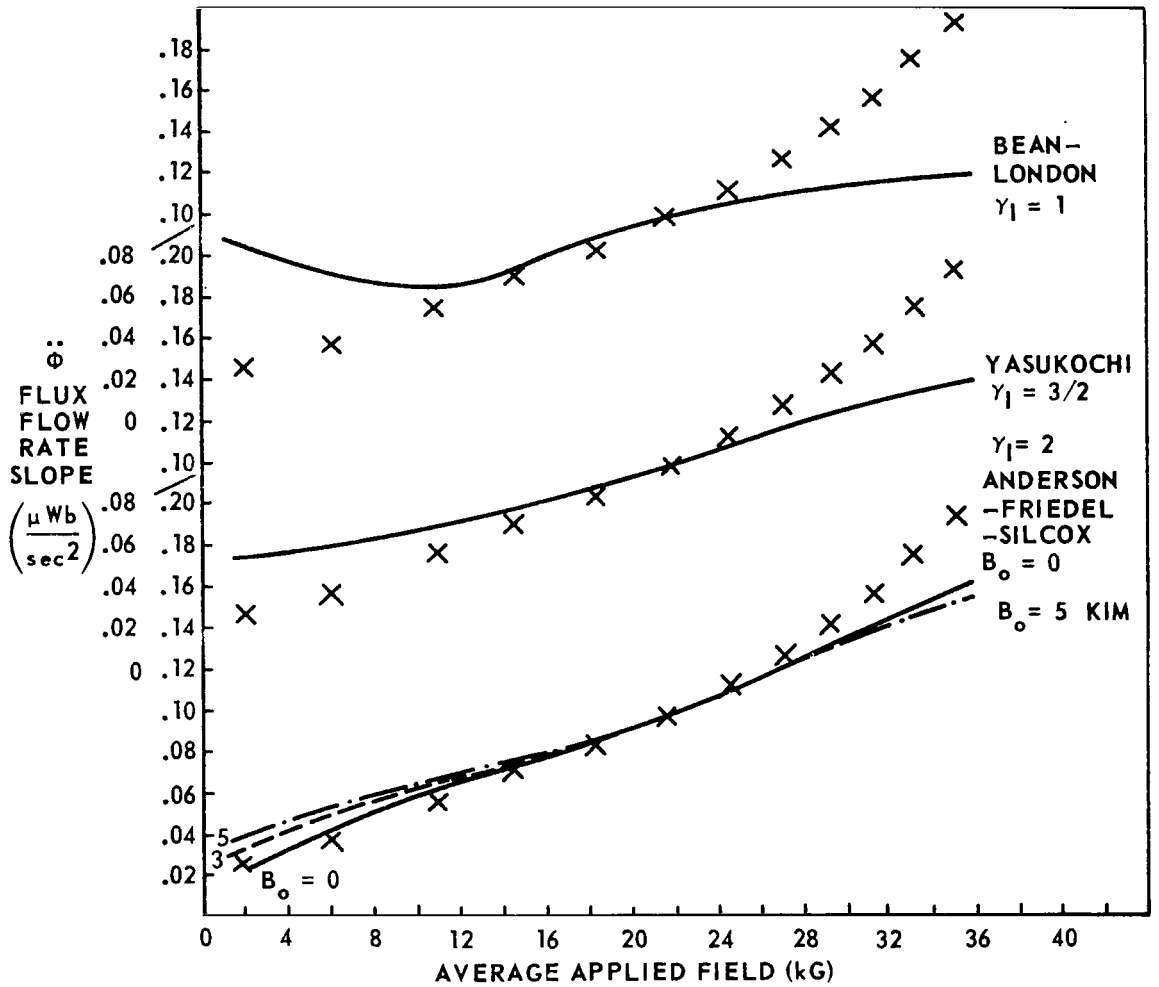

Figure 14. Flux flow rate slope calculations.

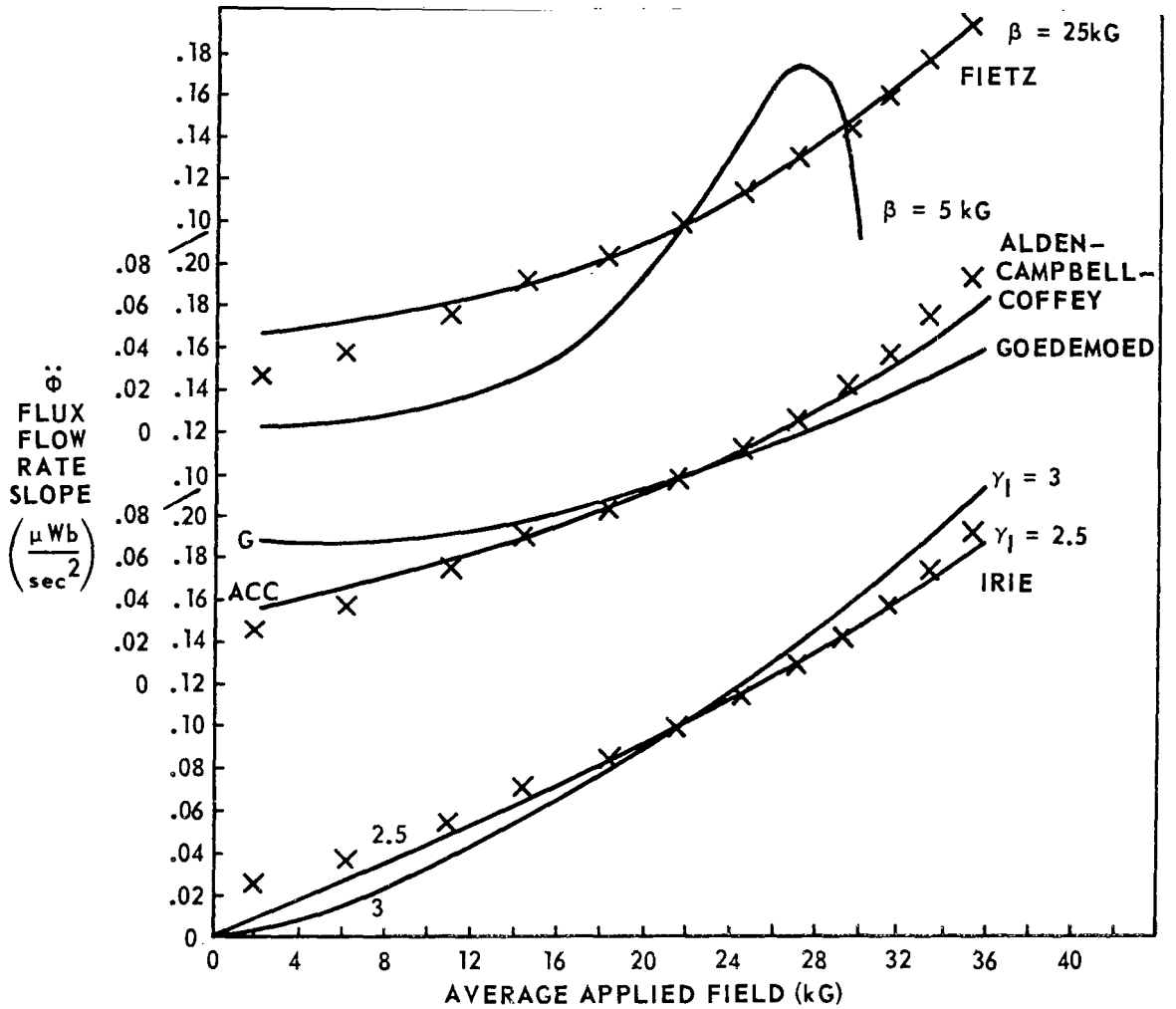

Figure 15. Flux flow rate slope calculations.

the Kim model are shown ($B_0 = 0$ gives the Anderson-Friedel-Silcox (AFS) result). For the Irie calculation, which reduces to the Bean-London, Yasukochi, and AFS curves for $\gamma = 1$, 3/2, and 2 respectively, only the curves for $\gamma = 2.5$ and 3 are shown. Note, however, that from Irie's original work there is no immediately apparent physical explanation for $\gamma > 2$. For the Goedemoed and the Alden-Campbell-Coffey (ACC) calculations, H_{c2} was taken as 63.6 kG, a measured value discussed in Appendix A.

The $\ddot{\phi}$ computation for the Fietz model with its three adjustable parameters was made as follows. It was required that J_c go to zero at H_{c2}, a necessary condition which Fietz et al. did not use in their work. This gave the result that $\gamma = -\alpha \exp\left(-\frac{\mu_0 H_{c2}}{\beta}\right)$, leaving two parameters α and β. In their paper Fietz et al. empirically found β to be of the order of 5 kG for two coils wound of Nb25%Zr wire. Therefore, $\beta = 5$ kG was chosen and the computation was fit at point A as usual, giving the strange behavior of Figure 15. Larger values of β were then chosen, in order to obtain a fit to the data at point B of Figure 12, as well as at point A. The very good fit in Figure 15 resulted when $\beta = 25$ kG. This value is so far from those measured by Fietz that the agreement must be considered as physically inexplicable as is the agreement of the Irie computation for $\gamma > 2$.

The apparent variation of the Bean-London (BL) curve with H is spurious. The BL expression for $\ddot{\phi}$ depends on H_a, but not on H_j, so the experimental variation of the size of the jump intervals leads to an apparent variation of $\ddot{\phi}$. This effect undoubtedly affects the curves of the other models but to a much smaller degree.

If the Fietz model is disregarded because of its unrealistic value of β , ACC results in the best empirical fit over the widest field range. Nevertheless, the calculated $\ddot{\phi}$ is 30 percent high at the lowest field jump and about 8 percent low at the highest field jump.

NEW CRITICAL CURRENT DENSITY MODEL

The unsatisfactory agreement with the present experiment of the flux flow calculations for all of the eight published critical current density functions (Table 1) led us to seek a better functional form for J_c. Since it appeared that a probable source of the failure of the models might be the assumption that α is independent of field, the variation of α with B was determined explicitly. Choosing the Kim model as a starting point, the successive values of α required to match the $\dot{\phi}$ formula to the series of measured interjump flow voltage variations were calculated. These α's are plotted against average applied field in Figure 16. By means of a least squares curve fit they are shown to lie approximately on a straight line which approaches zero at about 61 kilogauss. Because this maximum field is of the order of magnitude of H_{c2}, it appeared reasonable to assume that $\alpha(B)$ for the Kim model varies as

$$\alpha(B) = \alpha_c(\mu_0 H_{c2} - B) \quad , \tag{12}$$

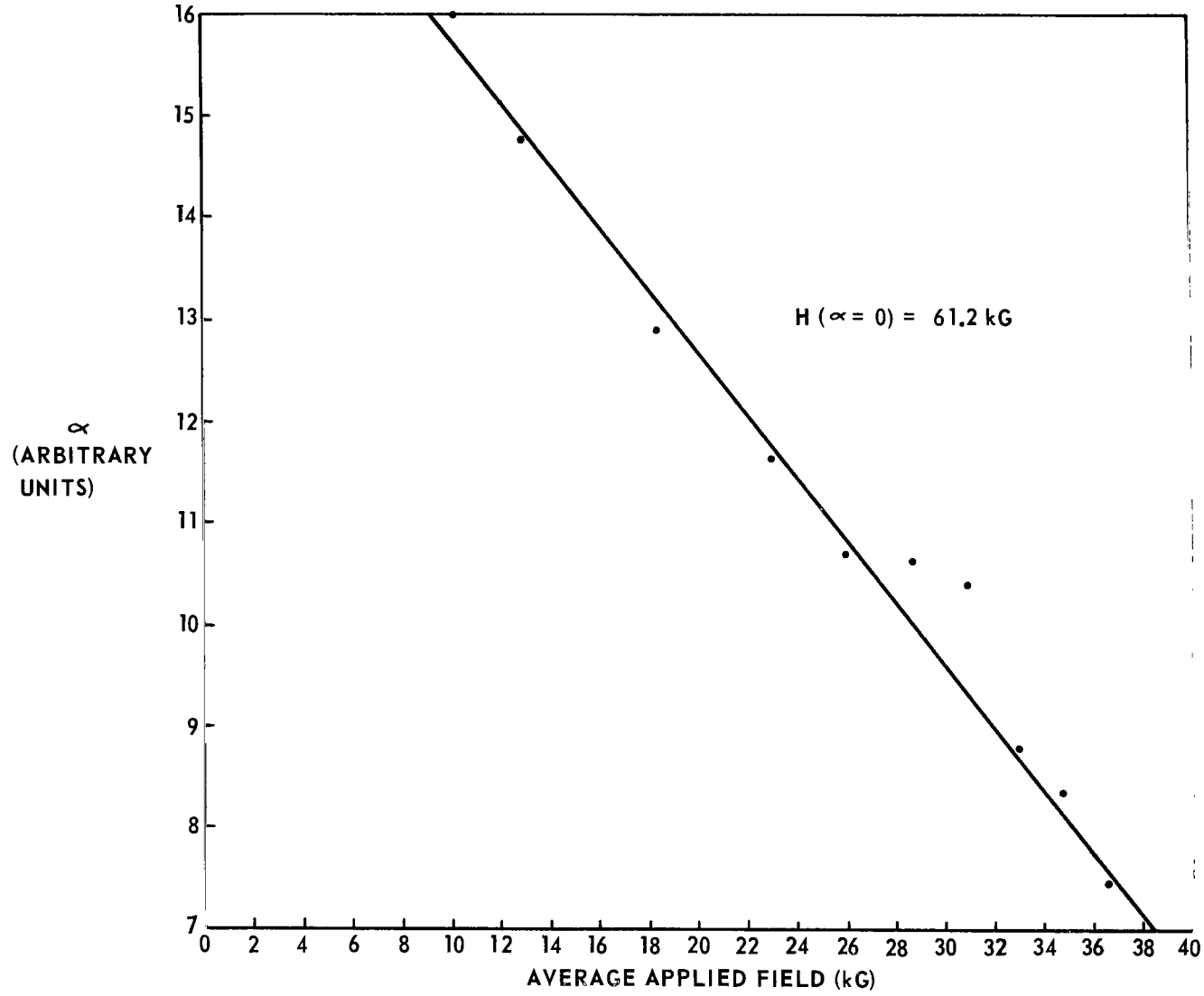

Figure 16. Variation of Kim model α with field.

where α_c is a field independent, temperature dependent constant. Inserting equation (12) into the Kim function of Table 1 gives

$$J_c = \alpha_c \frac{H_{c2} - B}{B_0 + B} , \qquad (13)$$

a functional form which is seen to vanish at the upper critical field H_{c2} and to approach a large, finite value $\alpha_c \frac{\mu_0 H_{c2}}{B_0}$ at $B = 0$.

The proof of the validity of this model lay, of course, in its ability to explain the present flux flow measurements and to agree at least reasonably well with other published results. Therefore, the total flux, flux flow, and flux flow slope calculations were made from equations (6), (8), (9), and (13). The results are summarized in Appendix C. H_{c2} was given its measured value of 63.6 kG (Appendix A). Here, we have two adjustable parameters, α_c and B_0, which were chosen to give exact empirical agreement of the $\dot{\phi}$ calculation with points A and B of Figure 11; for this fit, $\alpha_c = 3.3 \times 10^3$ A/cm^2 and $B_0 = 6.5$ kG. $\dot{\phi}$ curves were then calculated for all of the flux flow slope data of Figures 11, 12, and 13. The results shown in Figures 17 and 18 agree remarkably well with the measurements. We may, therefore, conclude that equation (13) is a very good representation of the field dependence of the critical current density, at least for Nb25%Zr. It remains, of course, to determine the validity of equation (13) for other Type II materials.

It is possible to verify the choices of α_c and B_0 made from the flow slope considerations by means of an independent experimental measurement. In Figure 5 it is observed that when $H = H_s$, the flux distribution $B_s(r)$ just

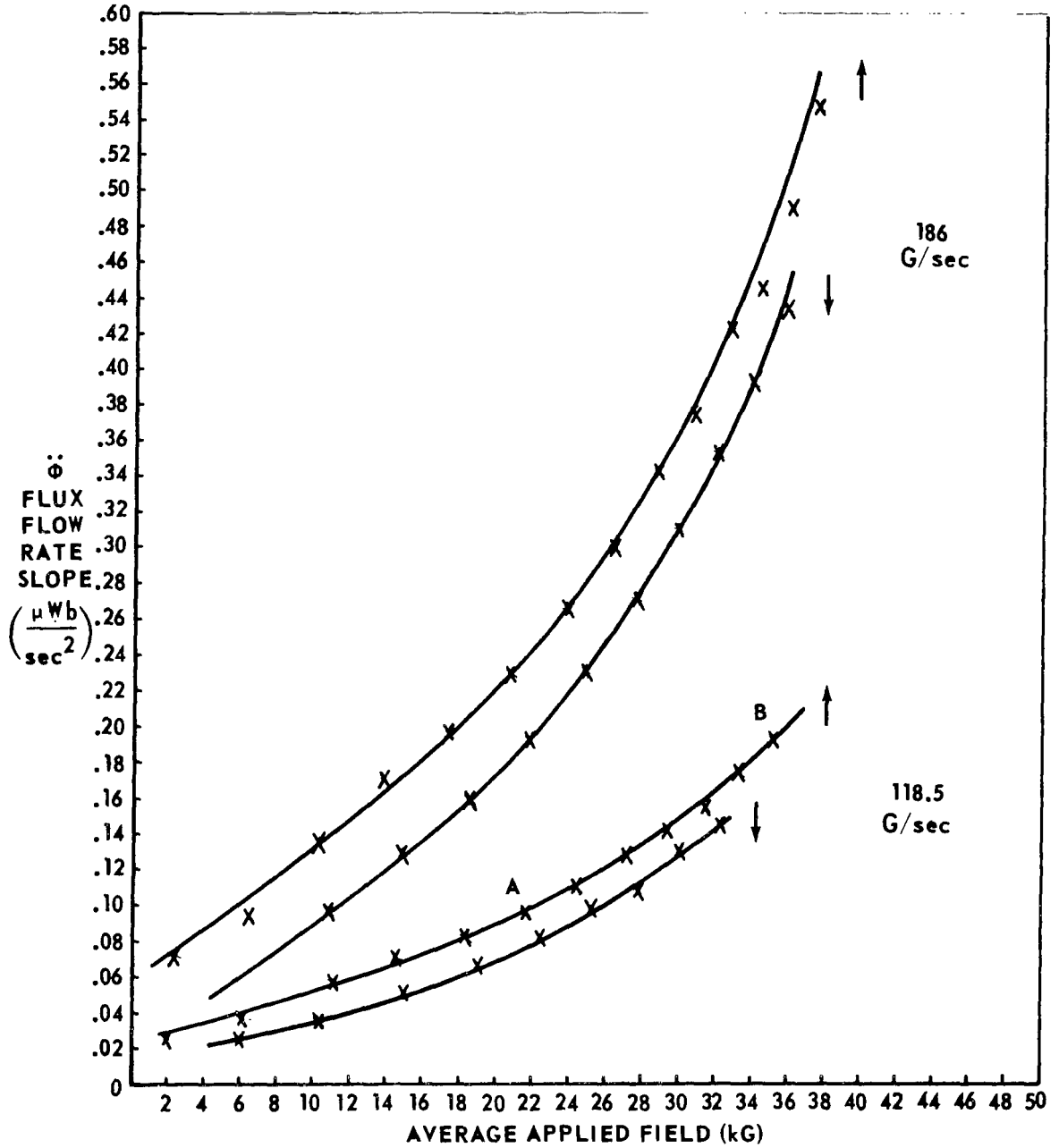

Figure 17. Flux flow rate slope calculation; new model.

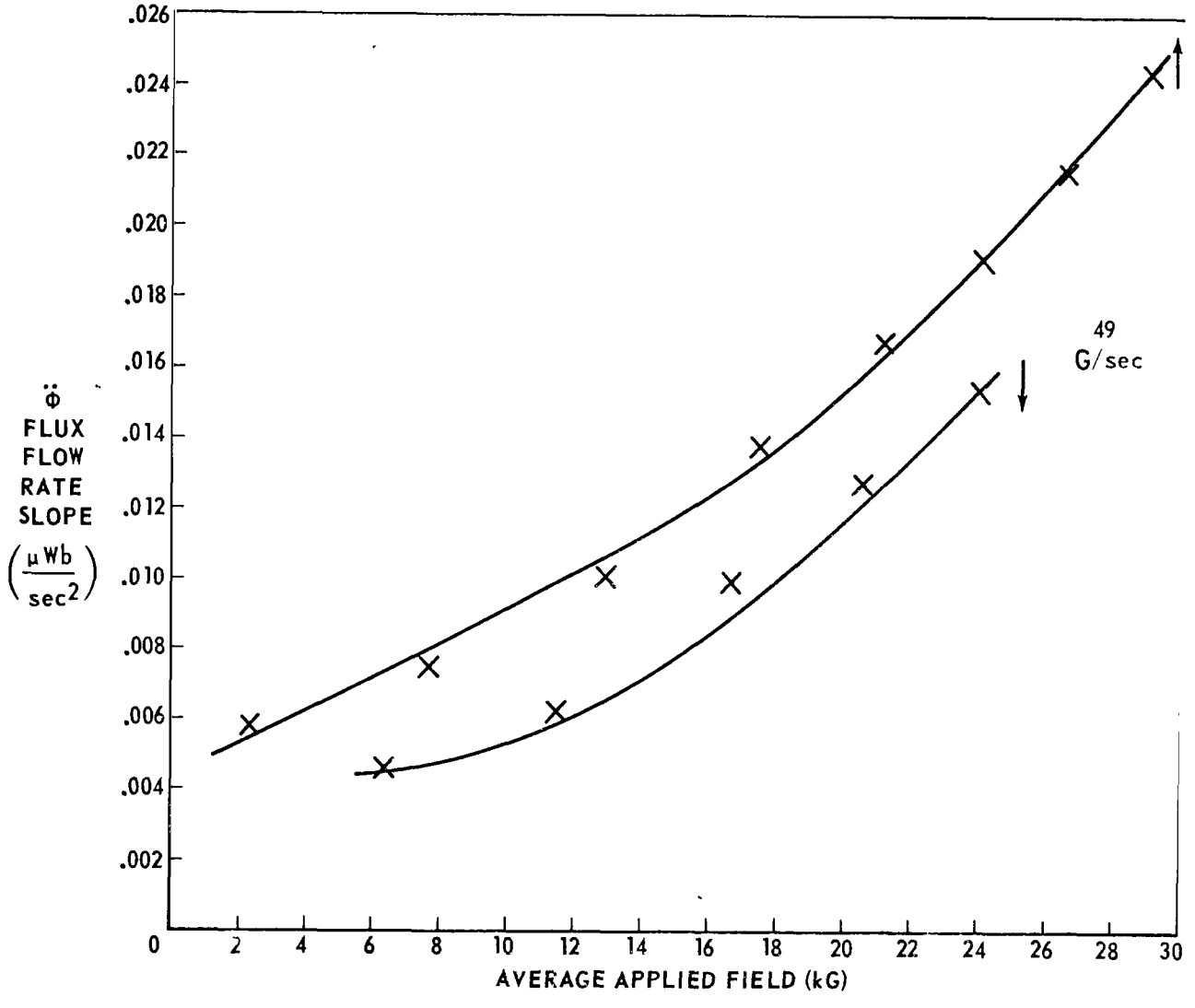

Figure 18. Flux flow rate slope calculation; new model; $\dot{H} = 49$ G/s.

reaches the tube bore. It follows that $r_{min} = b$ at that field. Subsequent increase of H causes flux to enter the bore and H' begins to increase. During the flux flow experiments, a similar sequence occurs each time the flux front starts from H_j and reaches the tube bore without a flux jump having previously disturbed the B distribution. Figure 19 shows an experimental H' versus H curve taken for $\dot{H} = 20$ G/s. At points E, G, and I, the flux front clearly reached the bore and H' increased, if only briefly. From the expression for r(B) in Appendix C and using the original values of H_{c2}, α_c, and B_0, we calculated the radial variation of B for selected values of H_j and H_a to match the fields on the increasing field portion of Figure 19. The B results are shown in Figure 20. Note that the calculated B curves reach the bore at the exact fields observed in the experiment. This confirms the empirical choice of α_c and B_0 from the fit to the flux flow slope results. Note also that flux jump number 2 initiates just as the flux front reaches the bore wall. This last observation directly confirms earlier suggestions [5] that a hollow superconductor is especially susceptible to flux jumps just when a sudden increase of flux flow must occur to permit the entire bore to begin to fill with additional field. Heating in the specimen, resulting from the more rapid flow, reduces the pinning forces and a jump may ensue.

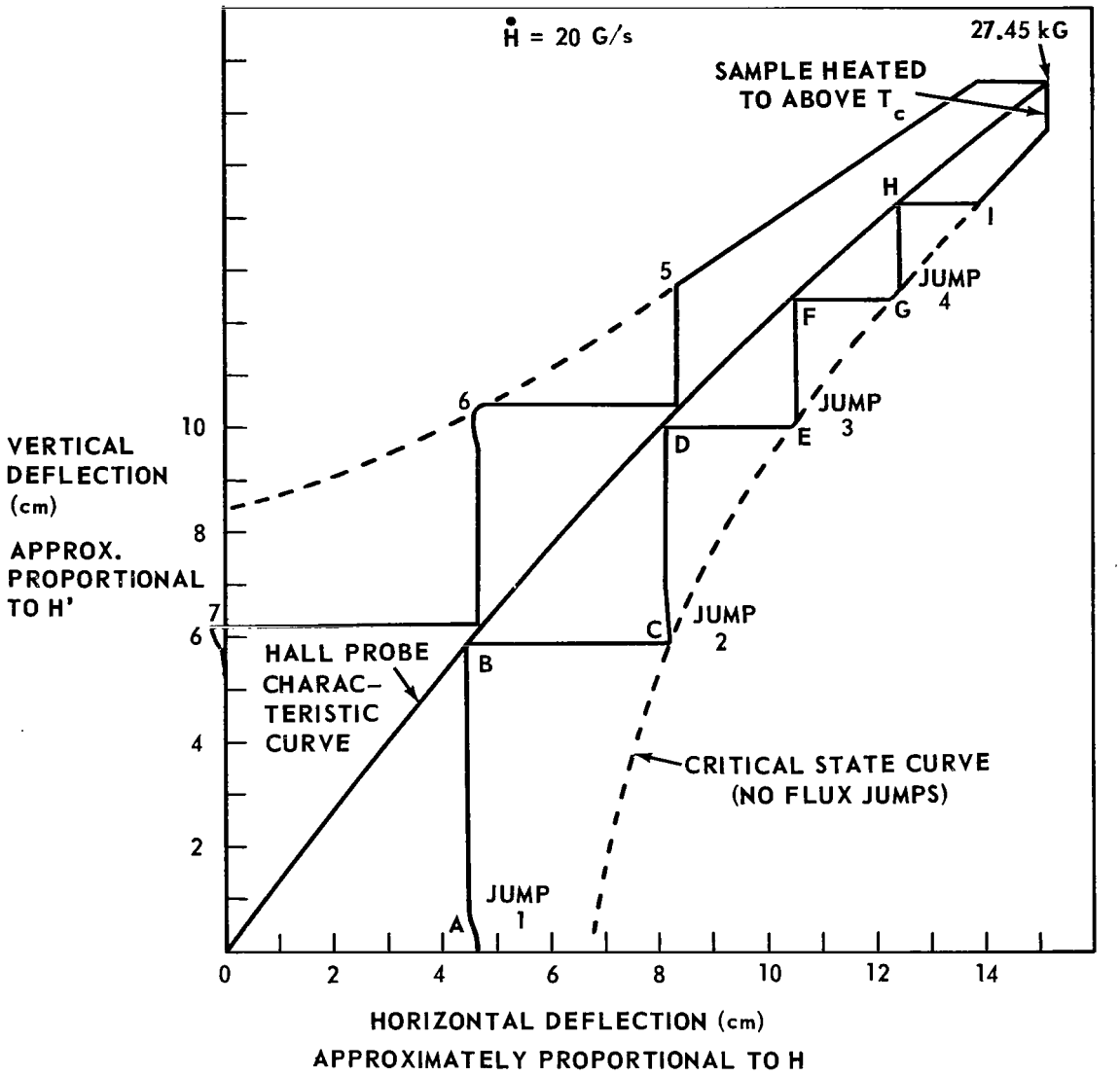

Figure 19. X-Y record of bore and applied fields; $\dot{H}$ = 20 G/s.

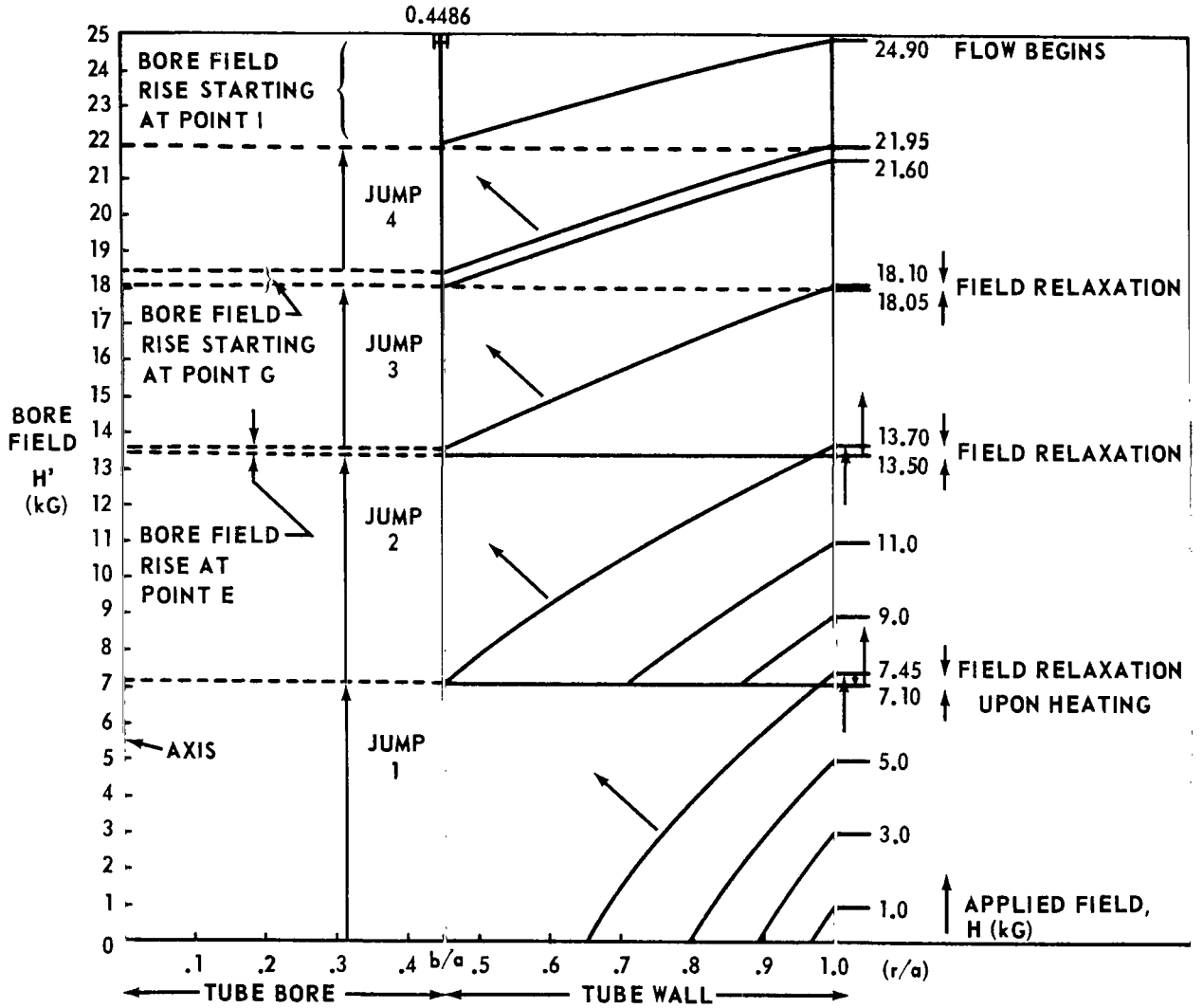

Figure 20. Induction in tube wall for experiment of Figure 19; calculated from new model.

Thus far, solutions to the very complicated formulas for $\ddot{\phi}$ given in Appendices B and C have been obtained. It is instructive to consider the behavior of the critical current functions which served as the starting point of each flux flow calculation. Using the values of the various parameters which gave the curves of Figures 14 and 15, the J_c curves for all of the models except that of Irie are plotted in Figures 21 and 23. If J_c for the new model is taken as the correct value for the present sample, the deviations of the different J_c models can be seen to reflect the deviations from the experimental results in Figures 14 and 15.

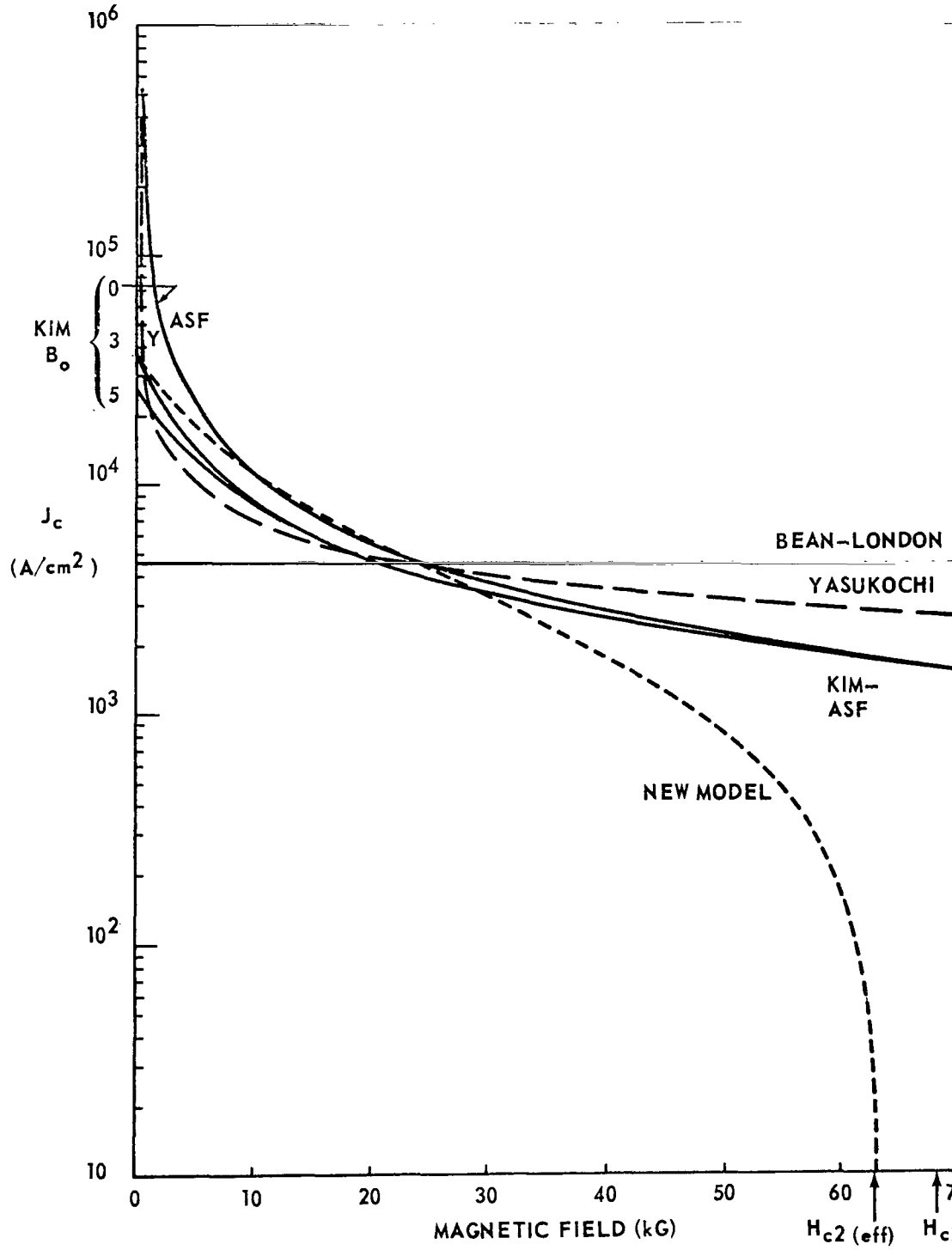

Figure 21. Critical current density functions with improper high field behavior.

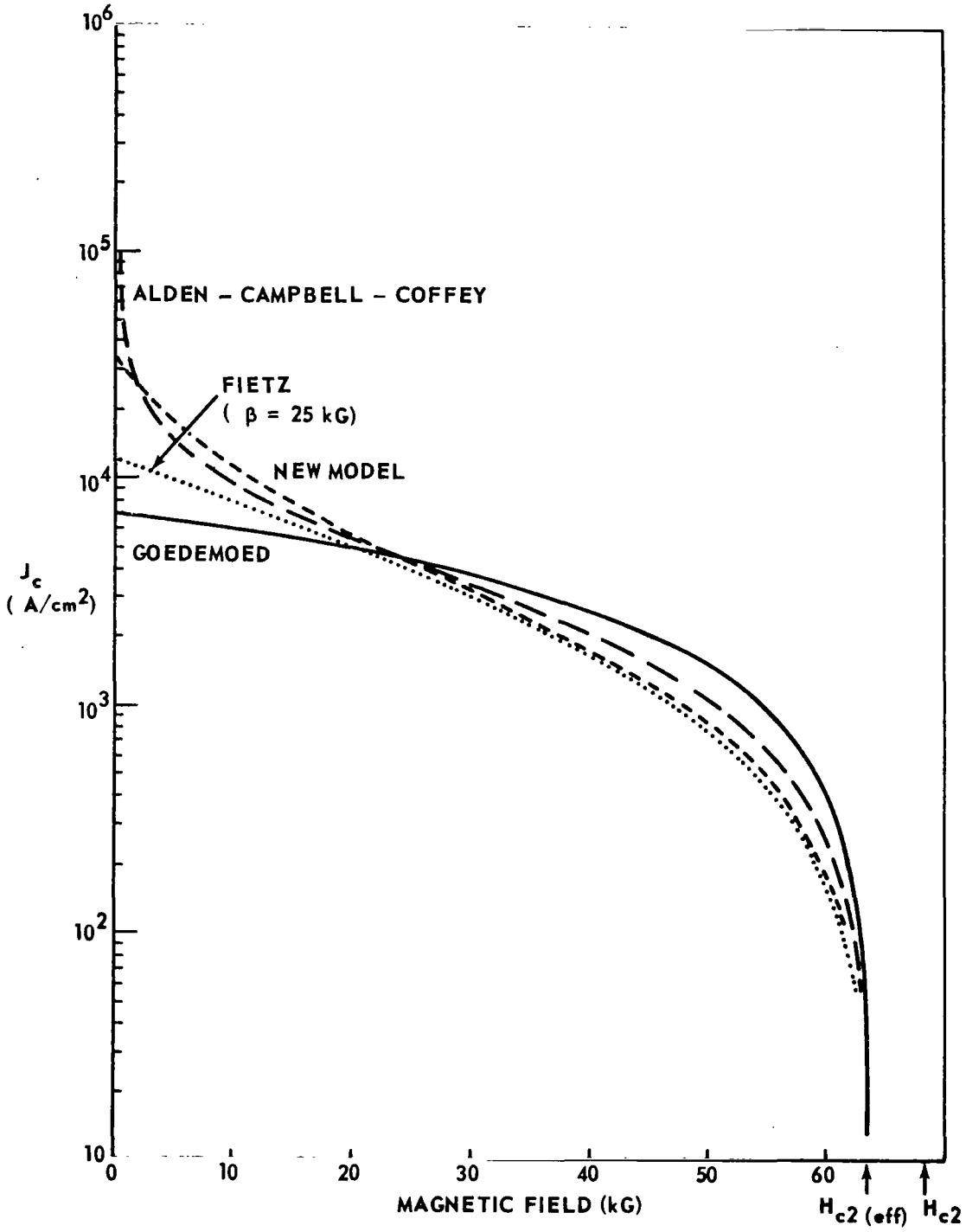

Figure 22. Critical current density functions with proper high field behavior.

DISCUSSION OF THE NEW MODEL

Equation (13) was found empirically and a physical basis for it remains to be established. In particular the significance of the constant B_0 is as obscure for the new model as it has been since it was originally introduced by Kim [9] (Table 1). It is striking, though perhaps only fortuitous, that the value of B_0 is just that field at which the flux flow rates for the continuous field sweep have a relative maximum (Fig. 7).

It is interesting to compare the Goedemoed and Alden-Campbell-Coffey critical current formulas with the new one (N). At low fields where $\mu_0 H_{c1} < B << \mu_0 H_{c2}$ the three current density models vary as $\mu_0 H_{c2}$, $\mu_0 H_{c2} B^{-1/2}$, and $\mu_0 H_{c2}(B_0 + B)^{-1}$ for G, ACC, and N respectively. Above H_{c1}, which is of the order of a few hundred gauss for Nb25%Zr, the Lorentz force or pinning force functions then vary as $\mu_0 H_{c2} B$, $\mu_0 H_{c2} B^{1/2}$, and $\mu_0 H_{c2} \left(\frac{B}{B_0 + B}\right)$ respectively. The low field importance of B_0 in the new model is apparent.

At high fields where B_0 may be neglected, the three forms may be summarized as $J_c \sim (\mu_0 H_{c2} - B) B^{-n}$, where $n = 0,\ 1/2,\ 1$ for G, ACC, and N respectively.

The n dependence can be seen in Figure 22 near H_{c2}. The Lorentz force and the net pinning force at high fields are then

$$F_L = F_p \sim (\mu_0 H_{c2} - B)B^{1-n} \quad ; \quad B >> B_0 \quad , \tag{14}$$

and for N they vary as $\mu_0 H_{c2} - B$. Coffey [21] has calculated that the fraction of the specimen cross section which is outside the fluxoid cores and remains superconducting is also proportional to $\mu_0 H_{c2} - B$. Consequently only the new model is seen to be consistent with the quite reasonable argument that the net pinning force on the fluxoids varies directly with the local area density of superconducting phase in the material.

SUMMARY

In this report we have discussed new observations of magnetic flux flow behavior in the Type II superconductor Nb25%Zr. The rate of flux flow $\dot{\phi}$ into or out of a cylindrical specimen increases linearly with field in the interval between flux jumps, provided the process in each interval starts from a condition of constant induction throughout the specimen. The slopes of the linearly increasing flow rates, which represent $\ddot{\phi}$, are themselves increasing functions of average applied field. Since the flux in the sample and its derivatives with respect to time can be calculated from an assumed variation of critical current density $J_c(B)$, it is possible to study the applicability of various functional forms of J_c which have been proposed in the literature. Although some of the eight previously advanced J_c models were able to explain the present data only over limited ranges of applied field, a new empirical model proposed and discussed in this report is shown to agree with the experimental results at all fields, except near H_{c2} where anomalous behavior occurs. The new model, $J_c = \alpha_c \frac{\mu_0 H_{c2} - B}{B_0 + B}$, is well behaved at very low fields and vanishes properly at H_{c2}. At intermediate fields, its variation closely resembles short sample critical

current densities reported in the literature. Although the physical significance of the constant B_0 remains obscure, its empirical value 6.5 kG is close to the values found for this parameter in the simpler, related Kim model. It remains to provide an explanation of the new model from considerations of microscopic flux pinning interactions in the superconductor.[8]

---

8. Portions of the work discussed here are also reported in Reference 22.

APPENDIX A
EXPERIMENTAL DETAILS AND ADDITIONAL MEASUREMENTS

Because some relatively novel experimental problems were encountered in this study and because the special dc amplification system used in the flow measurements has very good accuracy, sensitivity, and general utility, a more detailed discussion of the apparatus will be given.

The flux flow measurement system employed for this study was in effect a dual, rapid, high gain integrating digital voltmeter with simultaneous digital and analog output records. One channel was used for the outer flux flow pickup coil, the other for the inner coil; one channel is described. All of the apparatus in this dc amplifier was standard Hewlett-Packard instrumentation, but its use in the present system combination is noteworthy. A 2212A Voltage-to-Frequency Converter (VFC) converted the low level dc signal into a pulse train whose repetition frequency was directly proportional to the input voltage. The VFC sensitivity was 10 Hz per μV. The VFC pulse frequency output was counted by a 5321B Frequency Counter at a rate of 10 frequency readings per second. These frequencies corresponded to the average input voltage in microvolts during the counting time. They were digitized and recorded on one of two channels of a 5050B Digital Printer. A

temporary data storage feature in the printer reduced the time during which the printer inhibited the counter to 100 μs per print cycle. Consequently the system monitored the input signal 99.90 percent of the time and the probability was very small that any significant data fluctuations, including flux jumps, would be missed.

As they were recorded digitally, the frequency data were also fed to a 581A Digital-to-Analog Converter (DAC) which generated a dc voltage proportional to the number represented by the three least significant digits of each counter reading. This voltage was recorded on a 7100A Strip Recorder whose full scale deflection was adjusted to match the DAC output voltage range for a 0 to 999 reading. Thus, although the counter readings were often greater than 999, the recorder pen always remained on scale by recycling as often as necessary. Note, for example, the 636 μV and 1778 μV deflections in Figure 10. It can be seen that this method effectively expanded the width of the final analog recording, while maintaining the same absolute sensitivity. Ambiguities introduced by pen recycling were removed later by reference to the digital record. Introduction of the 0.1 second integration time into the data produced small, unobtrusive steps in the final analog record, as was seen in Figures 6 and 10.

To eliminate thermoelectric voltage problems in the flux flow measurements, the pickup coils were formed of a continuous conductor from one room temperature VFC input through the coil winding in the liquid helium and back to the other VFC input. The VFC-to-coil connections

themselves were enclosed in a cardboard box to protect them from rapid temperature changes. Drifts in the entire system were very slow and could easily be corrected for by occasionally rezeroing the VFC's.

Although the field sweep rates were automatically and very accurately controlled at intermediate magnetic fields by the magnet power supply, problems were encountered at low (< 8 kG) and very high (> 36 kG) fields. In these regions for $\dot{H} > 0$, the magnet sweep rate changed in a slow, reproducible manner because of changing magnetic inductance. These anomalous sweep rates were independently measured by means of a bare copper coil in the solenoid bore and the data plotted in Figures 11 through 14 and 16 through 17 were corrected accordingly. The data in these figures accurately reflect the flow slope behavior which would be observed for the stated constant $\dot{H}$ values.

Since one parameter of three of the important critical current models considered in this report is the upper bulk critical field H_{c2}, its direct measurement was necessary. Published values [23] of H_{c2} for Nb25%Zr are spread around 70 kG and have large uncertainties. Since H_{c2} is a function of composition, and the exact composition for this specimen was not known, an independent critical field determination was made. Under normal circumstances H_{c2} is the field at which the sample becomes normal and the difference $H' - H$ between the bore and applied fields becomes zero. Since both branches of the critical state curve converge to $H' = H$ at H_{c2}, the upper critical field is observed as the field at which the two branches merge with the $H' = H$ Hall probe characteristic.

The NbZr sample studied exhibits an interesting property known as the peak effect. It is common to many Type II materials and has been attributed [24] to increasing resistance to mutual interpenetration by the flux lines in the sample near H_{c2}. Its existence necessitates the definition of two upper critical fields. High field H' versus H data are shown in Figure A-1 in which the peak effect is quite evident; at several fields on both critical state curves the slow sweep was stopped and the sample heated to above T_c to define the Hall probe characteristic.

Above approximately 55 kG for $\dot{H} > 0$ the field difference $H' - H$, instead of continuing to converge monotonically toward zero, begins to increase with field. It passes through a maximum and then falls rather rapidly to zero. For $\dot{H} < 0$, a similar maximum in $H' - H$ is seen. This rapid high field convergence of the critical state envelopes permits relatively precise determination of the true bulk upper critical field, which will be simply referred to as H_{c2}. One would expect that any reasonably simple physical model which explains the magnetization and flux flow data at fields below 55 kG should extrapolate smoothly into the region in which the peak effect is observed. It follows that the value of upper critical field which must be used in such a model is that field toward which the magnetization is converging when the peak effect commences. This effective bulk upper critical field will be called $H_{c2(eff)}$.

To allow estimation of H_{c2} and $H_{c2(eff)}$ the X-Y recorder pen separation at constant H was plotted from approximately 38 kG to H_{c2}

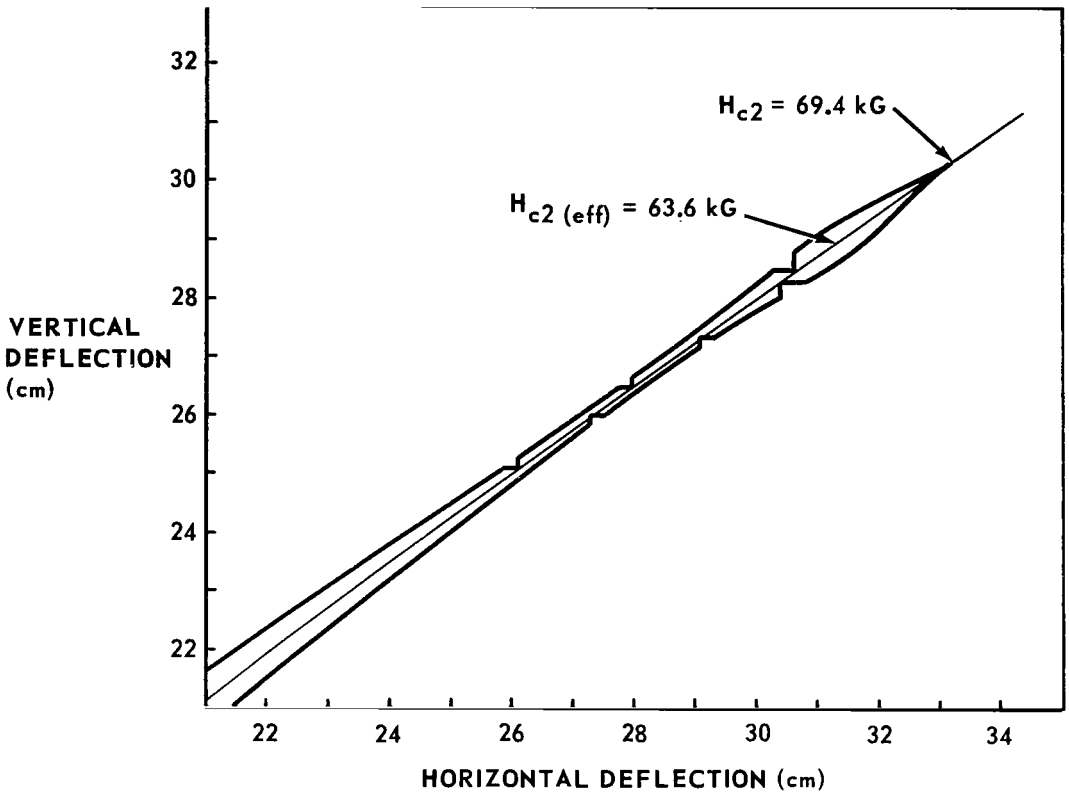

Figure A-1. X-Y record of bore and applied fields near H_{c2}.

as seen in Figure A-2. The peak effect is very pronounced and at its high field side drops steeply and smoothly to an intercept at 69.4 ± 0.1 kG. A very linear decrease occurs prior to the onset of the peak effect rise. A linear least squares curve fit leads to an extrapolated effective value $H_{c2(eff)}$ of 63.6 ± 0.5 kG, the value which was used above in the fit of the critical current density models to the flux flow data.

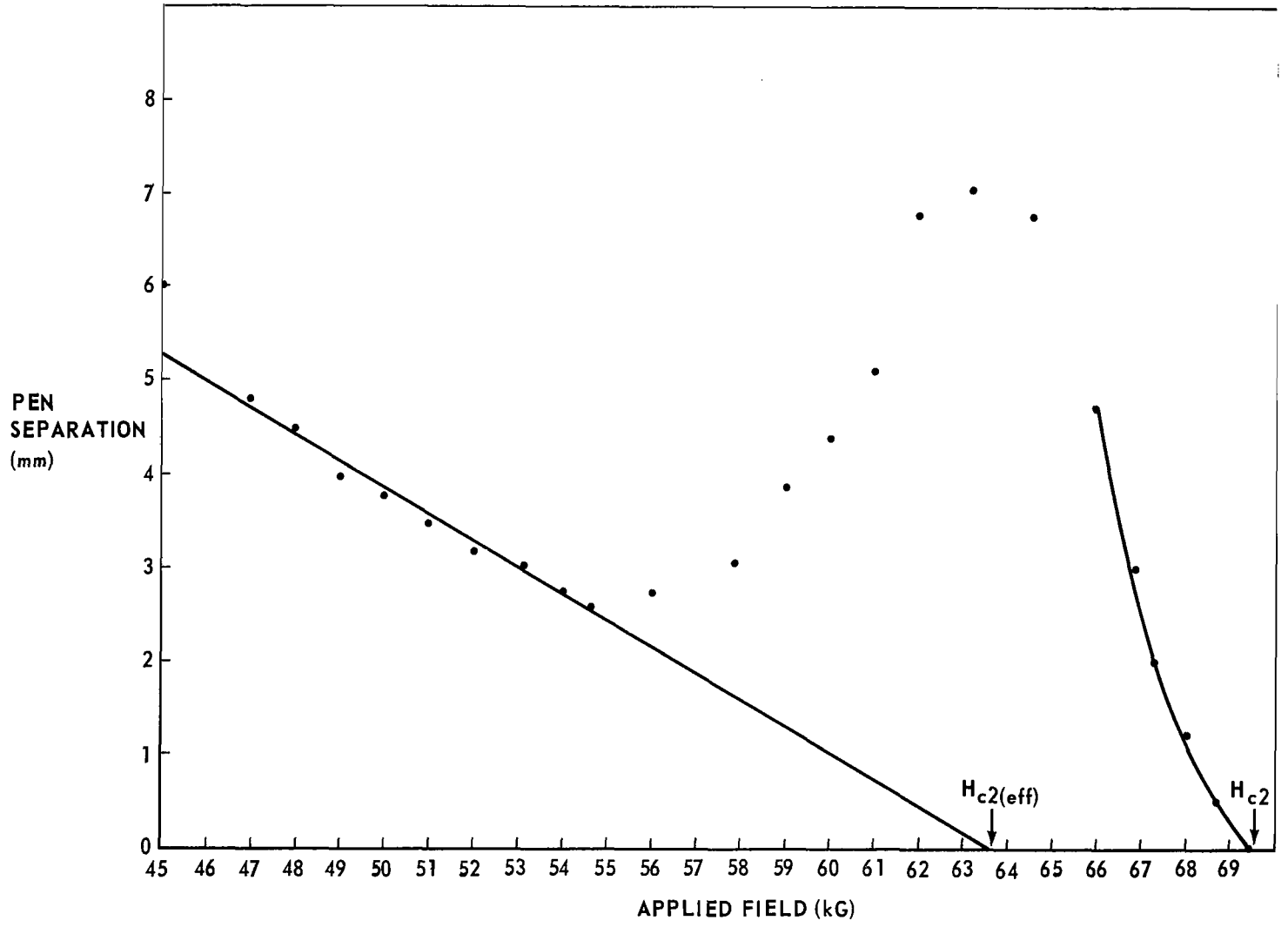

Figure A-2. X-Y pen separation near H_{c2}.

APPENDIX B

CALCULATION RESULTS – PUBLISHED MODELS

Bean-London Model

$$J_c = \alpha = \mp \alpha_c = \text{constant} \quad ; \quad [\alpha] = A/m^2 \tag{B-1}$$

$$r_{min} = a - \frac{H_a}{\alpha_c} \tag{B-2}$$

$$B(r,t) = \mp \mu_0 \alpha_c (a - r) + \mu_0 (H_j \pm H_a) \tag{B-3}$$

$$\phi(t) = \mu_0 \pi a^2 H_j \pm \frac{\mu_0 \pi}{\alpha_c^2} \left\{ \alpha_c a H_a^2 - \frac{1}{3} H_a^3 \right\} \tag{B-4}$$

$$\dot{\phi}(t) = \pm \frac{\mu_0 \pi}{\alpha_c^2} \dot{H} \left\{ 2 \alpha_c a H_a - H_a^2 \right\} \tag{B-5}$$

$$\ddot{\phi}(t) = \pm \frac{2 \mu_0 \pi}{\alpha_c^2} \dot{H}^2 \left\{ \alpha_c a - H_a \right\} \tag{B-6}$$

Kim Model (B_0)

Anderson-Friedel-Silcox Model ($B_0 = 0$)

$$J_c = \frac{\alpha}{B_0 + B} = \mp \frac{\alpha_c}{B_0 + B} \quad ; \quad [\alpha] = \frac{AWb}{m^4} \tag{B-7}$$

$$r_{min} = a - \frac{H_a}{\alpha_c} \left\{ \frac{\mu_0}{2} (2H_j \pm H_a) + B_0 \right\} \tag{B-8}$$

$$B(r,t) = \left\{ \left[\mu_0 (H_j \pm H_a) + B_0 \right] \mp 2\mu_0 \alpha_c (a - r) \right\}^{1/2} - B_0 \qquad \text{(B-9)}$$

$$\phi(t) = \mu_0 \pi a^2 H_j + \frac{\pi \mu_0}{\alpha_c^2} \left\{ \pm \alpha_c a \left[(\mu_0 H_j + B_0) H_a^2 \pm \frac{2}{3} \mu_0 H_a^3 \right] \right.$$

$$\mp \frac{1}{3} (\mu_0 H_j + B_0)^2 H_a^3 - \frac{5}{12} \mu_0 (\mu_0 H_j + B_0) H_a^4$$

$$\left. \mp \frac{2}{15} \mu_0^2 H_a^5 \right\} \qquad \text{(B-10)}$$

$$\dot{\phi}(t) = \pm \frac{\pi \mu_0}{\alpha_c^2} \dot{H} \left\{ 2 \alpha_c a \left[(\mu_0 H_j + B_0) H_a \pm \mu_0 H_a^2 \right] - (\mu_0 H_j + B_0)^2 H_a^2 \right.$$

$$\left. \mp \frac{5}{3} \mu_0 (\mu_0 H_j + B_0) H_a^3 - \frac{2}{3} \mu_0^2 H_a^4 \right\} \qquad \text{(B-11)}$$

$$\ddot{\phi}(t) = \frac{\pi \mu_0}{\alpha_c^2} \dot{H}^2 \left\{ \pm 2 \alpha_c a \left[(\mu_0 H_j + B_0) \pm 2 \mu_0 H_a \right] \right.$$

$$\mp 2 (\mu_0 H_j + B_0)^2 H_a - 5 \mu_0 (\mu_0 H_j + B_0) H_a^2$$

$$\left. \mp \frac{8}{3} \mu_0^2 H_a^3 \right\} \qquad \text{(B-12)}$$

Irie Model (Y)

Bean Model (Y = 1)

Yasukochi Model $\left(\gamma = \frac{3}{2}\right)$

Anderson-Friedel-Silcox Model (Y = 2)

$$J_c = \frac{\alpha}{B^{\gamma-1}} = \mp \frac{\alpha_c}{B^{\gamma-1}} \quad ; \quad [\alpha] \ \frac{A}{m^2} \left(\frac{Wb}{m^2} \right)^{\gamma-1} \qquad \text{(B-13)}$$

where γ = constant

$$r_{min} = a \mp \frac{\mu_0^{\gamma-1}}{\alpha_c \gamma} \left[(H_j \pm H_a)^{\gamma} - H_j^{\gamma} \right] \tag{B-14}$$

$$B(r,t) = \left\{ \mp \mu_0 \alpha_c \gamma (a - r) + \mu_0^{\gamma} (H_j \pm H_a)^{\gamma} \right\}^{1/\gamma} \tag{B-15}$$

$$\begin{aligned} \phi(t) = \mu_0 \pi a^2 H_j + \frac{2\pi \mu_0^{2\gamma}}{\alpha_c^2 \gamma} \Bigg\{ & \mp \mu_0^{1-\gamma} \alpha_c a \left[H_j \left[(H_j \pm H_a)^{\gamma} - H_j^{\gamma} \right] \right. \\ & \left. - \frac{\gamma}{\gamma+1} \left[(H_j \pm H_a)^{\gamma+1} - H_j^{\gamma+1} \right] \right] \\ & + \frac{1}{2\gamma(2\gamma+1)} H_j^{2\gamma+1} - \frac{1}{\gamma(\gamma+1)} H_j^{\gamma+1} (H_j \pm H_a)^{\gamma} \\ & + \frac{1}{2\gamma} H_j (H_j \pm H_a)^{2\gamma} \\ & - \frac{\gamma}{(\gamma+1)(2\gamma+1)} (H_j \pm H_a)^{2\gamma+1} \Bigg\} \end{aligned} \tag{B-16}$$

$$\begin{aligned} \dot{\phi}(t) = \pm \frac{2\pi \mu_0^{2\gamma-1}}{\alpha_c^2 \gamma} \dot{H} \Bigg\{ & \mp \mu_0^{1-\gamma} \gamma \alpha_c a \left[H_j (H_j \pm H_a)^{\gamma-1} - (H_j \pm H_a)^{\gamma} \right] \\ & - \frac{1}{\gamma+1} H_j^{\gamma+1} (H_j \pm H_a)^{\gamma-1} + H_j (H_j \pm H_a)^{2\gamma-1} \\ & - \frac{\gamma}{\gamma+1} (H_j \pm H_a)^{2\gamma} \Bigg\} \end{aligned} \tag{B-17}$$

$$\begin{aligned} \ddot{\phi}(t) = \frac{2\pi \mu_0^{2\gamma-2}}{\alpha_c^2 \gamma} \dot{H}^2 \Bigg\{ & \mp \mu_0^{1-\gamma} \gamma \alpha_c a \left[(\gamma-1) H_j (H_j \pm H_a)^{\gamma-2} - \gamma (H_j \pm H_a)^{\gamma-1} \right] \\ & - \frac{\gamma-1}{\gamma+1} H_j^{\gamma+1} (H_j \pm H_a)^{\gamma-2} + (2\gamma-1) H_j (H_j \pm H_a)^{2\gamma-2} \\ & - \frac{2\gamma^2}{\gamma+1} (H_j \pm H_a)^{2\gamma-1} \Bigg\} \end{aligned} \tag{B-18}$$

Goedemoed Model

$$J_c = \alpha(\mu_0 H_{c2} - B) = \mp \alpha_c(\mu_0 H_{c2} - B) \quad ; \quad [\alpha] = \frac{A}{Wb} \tag{B-19}$$

$$r_{min} = a \mp \frac{1}{\mu_0 \alpha_c} \ln\left(\frac{1 - x_j}{1 - x}\right) \tag{B-20}$$

where $$x = \frac{H_j \pm H_a}{H_{c2}} \quad , \quad x_j = \frac{H_j}{H_{c2}}$$

$$B(r,t) = \mu_0 H_{c2} \left\{ 1 - (1 - x) \exp\left[\mp \mu_0 \alpha_c (r - a)\right] \right\} \tag{B-21}$$

$$\phi(t) = \mu_0 \pi a^2 H_j + \frac{2\pi H_{c2}}{\mu_0 \alpha_c^2} \left\{ -\frac{1}{2}(1 - x_j)\left[\ln \frac{1 - x}{1 - x_j}\right]^2 \right.$$

$$\left. -(1 \mp \mu_0 \alpha_c a)\left[(1-x_j) \ln \frac{1 - x}{1 - x_j} - (x_j - x)\right] \right\} \tag{B-22}$$

$$\dot{\phi}(t) = \pm \frac{2\pi}{\mu_0 \alpha_c^2} \dot{H} \left\{ -(1 \mp \mu_0 \alpha_c a) \frac{x_j - x}{1-x} + \frac{1-x_j}{1-x} \ln \frac{1-x}{1-x_j} \right\} \tag{B-23}$$

$$\ddot{\phi}(t) = \frac{2\pi}{\mu_0 \alpha_c^2 H_{c2}} \dot{H}^2 \frac{1-x_j}{(1-x)^2} \left\{ \pm \mu_0 \alpha_c a + \ln \frac{1-x}{1-x_j} \right\} \tag{B-24}$$

Alden-Campbell-Coffey Model

$$J_c = \alpha \frac{\mu_0 H_{c2} - B}{B^{1/2}} = \mp \alpha_c \frac{\mu_0 H_{c2} - B}{B^{1/2}} \quad ; \quad [\alpha] = \frac{A}{m(Wb)^{1/2}} \tag{B-25}$$

$$r(\beta,t) = a \mp \frac{2}{\mu_0 \alpha_c} (\mu_0 H_{c2})^{1/2} \left[\beta^{1/2} - x^{1/2} - \tanh^{-1}(\beta^{1/2}) + \tanh^{-1}(x^{1/2})\right] \tag{B-26}$$

where $$x = \frac{H_j \pm H_a}{H_{c2}} \quad , \quad \beta = \frac{B}{\mu_0 H_{c2}}$$

$$r_{min} = r(\beta = x_j,\ t) \tag{B-27}$$

where $$x_j = \frac{H_j}{H_{c2}}$$

$$\phi(t) = \mu_0 \pi a^2 H_j + \frac{4\pi H_{c2}^2}{\alpha_c^2} \left\{ A + C x^{1/2} + \left(x_j - \frac{4}{3}\right)x \mp \frac{1}{3} \frac{\mu_0 \alpha_c a}{(\mu_0 H_{c2})^{1/2}} x^{3/2} \right.$$

$$- \frac{1}{6} x^2 + D \tanh^{-1}(x^{1/2}) - (1-x_j)\left[\tanh^{-1}(x^{1/2})\right]^2$$

$$\left. + 2(1-x_j) x^{1/2} \tanh^{-1}(x^{1/2}) - \frac{1}{3} \ln(x-1) \right\} \tag{B-28}$$

where A = 10 term constant (function of α_c, x_j)

C = 4 term constant (function of α_c, x_j)

D = 6 term constant (function of α_c, x_j)

$$\dot{\phi}(t) = \frac{4\pi H_{c2}}{\alpha_c^2} \dot{H} \frac{x^{1/2}}{1-x} \left\{ \mp \frac{1}{2} \alpha_c a \left(\frac{\mu_0}{H_{c2}}\right)^{1/2} (x_j - x) + \frac{2}{3} x_j^{3/2} - x_j^{1/2} \right.$$

$$+ (1-x_j)\left[\tanh^{-1}(x_j^{1/2}) - \tanh^{-1}(x^{1/2})\right]$$

$$\left. + (1-x_j) x^{1/2} + \frac{1}{3} x^{3/2} \right\} \tag{B-29}$$

$$\ddot{\phi}(t) = \frac{2\pi}{\alpha_c^2}\,\dot{H}^2\,\frac{x^{-1/2}}{(1-x)^2}\left\{ \mp\frac{1}{2}\,\alpha_c\, a\left(\frac{\mu_0}{H_{c2}}\right)^{1/2}\left[\, x_j(1+x) + x(x-3)\right] \right.$$

$$+ (1+x)(1-x_j)\left[\tanh^{-1}(x_j)^{1/2} - \tanh^{-1}(x)^{1/2}\right]$$

$$+ x^{1/2}(1-x_j) + \frac{2}{3}x^{3/2}(2-x)$$

$$\left. - x_j^{1/2}(1+x)\left(1 - \frac{2}{3}x_j\right)\right\} \qquad \text{(B-30)}$$

Fietz Model

$$J_c = \alpha \exp\left(-\frac{B}{\beta}\right) + \gamma = \mp\,\alpha_c \exp\left(-\frac{B}{\beta}\right) \mp \gamma_c \quad ; \quad [\alpha, \gamma] = \frac{A}{m^2} \qquad \text{(B-31)}$$

$$r(B,t) = a \mp \frac{\beta}{\mu_0\,\gamma_c}\left[\frac{B}{\beta} - x + \ln\frac{\gamma_c + \alpha_c \exp\frac{B}{\beta}}{\gamma_c + \alpha_c \exp(-x)}\right] \qquad \text{(B-32)}$$

where $\quad x = \mu_0\,\dfrac{H_j \pm H_a}{\beta}$

$$r_{min} = r\,(B = \mu_0 H_j,\ t) \qquad \text{(B-33)}$$

$$\dot{\phi}(t) = \pm\frac{\pi\beta^2}{\mu_0\,\gamma_c^2}\,\dot{H}\left\{ \mp\frac{2\,a\,\mu_0\,\gamma_c}{\beta}\left[\pm(x-x_j) + \ln\frac{\gamma_c + \alpha_c\exp(-x)}{\gamma_c + \alpha_c\exp(-x_j)}\right]\right.$$

$$\mp (x-x_j)^2 \mp 2(x-x_j)\ln\frac{\gamma_c + \alpha_c\exp(-x)}{\gamma_c + \alpha_c\exp(-x_j)}$$

$$\left. - \left[\ln\frac{\gamma_c + \alpha_c\exp(-x)}{\gamma_c + \alpha_c\exp(-x_j)}\right]^2\right\} \qquad \text{(B-34)}$$

where $\quad x_j = \mu_0\,\dfrac{H_j}{\beta}$

$$\ddot{\phi}(t) = \frac{2\,\pi\,\beta}{\gamma_c}\,\frac{\dot{H}^2}{\gamma_c + \alpha_c \exp(-x)}\left\{ \mp \frac{a\,\mu_0\,\gamma_c}{\beta} - (x - x_j) - \ln \frac{\gamma_c + \alpha_c \exp(-x)}{\gamma_c + \alpha_c \exp(-x_j)} \right\} \tag{B-35}$$

APPENDIX C

CALCULATION RESULTS – NEW MODEL

$$J_c = \alpha \frac{\mu_0 H_{c2} - B}{B_0 + B} = \mp \alpha_c \frac{\mu_0 H_{c2} - B}{B_0 + B} \quad ; \quad [\alpha] = \frac{A}{m^2} \tag{C-1}$$

$$r(\beta, t) = a \mp \frac{H_{c2}}{\alpha_c} \left\{ \beta - x + (1 + \beta_0) \ln \frac{1 - \beta}{1 - x} \right\} \tag{C-2}$$

where $x = \frac{H_j \pm H_a}{H_{c2}}$; $\beta = \frac{B}{\mu_0 H_{c2}}$, $\beta_0 = \frac{B_0}{\mu_0 H_{c2}}$

$$r_{min} = r(\beta = x_j, t) \tag{C-3}$$

where $x_j = \frac{H_j}{H_{c2}}$

$$\begin{aligned} \phi(t) = \mu_0 \pi a^2 H_j + \frac{\pi \mu_0 H_{c2}^3}{\alpha_c^2} \Bigg\{ \mp \frac{\alpha_c a}{H_{c2}} \Bigg[& (x - x_j)^2 + 2(1 + \beta_0)(x - x_j) \\ & + 2(1 + \beta_0)(1 - x_j) \ln \frac{1 - x}{1 - x_j} \Bigg] \\ & + A + C x + \left[x_j - \frac{3}{2}(1 + \beta_0) \right] x^2 - \frac{1}{3} x^3 \\ & + D \ln(1 - x) - (1 + \beta_0)^2 (1 - x_j) \left[\ln (1 - x) \right]^2 \\ & - 2(1 + \beta_0)(1 - x_j) \, x \ln (1 - x) \Bigg\} \end{aligned} \tag{C-4}$$

where A = 6 term constant (function of x_j, β_0)

C = 4 term constant (function of x_j, β_0)

D = 4 term constant (function of x_j, β_0)

$$\phi(t) = \frac{2\pi\mu_0 H_{c2}^2}{\alpha_c^2}\,\dot{H}\,(1+\beta_0)\left\{\pm\frac{\alpha_c a}{H_{c2}}\,\frac{x+\beta_0}{1+\beta_0}\cdot\frac{x-x_j}{1-x}+x_j-\frac{1}{2}(1+2\beta_0)\right.$$

$$-\frac{x_j^2}{2(1+\beta_0)}-(1-x_j)\ln\frac{1-x}{1-x_j}+\left[\frac{x_j}{1+\beta_0}-\frac{3}{2}\right]x$$

$$-\frac{x^2}{2(1+\beta_0)}+(1+\beta_0)\ln\frac{1-x}{1-x_j}+\frac{1-x_j}{1-x}\,x$$

$$\left.+\left[(x+\beta_0)+\frac{1}{2}(1-x_j)\right]\frac{1-x_j}{1-x}\right\} \qquad \text{(C-5)}$$

$$\ddot{\phi}(t) = \frac{2\pi\mu_0 H_{c2}}{\alpha_c^2}\,\dot{H}^2\,\frac{1+\beta_0}{(1-x)^2}\left\{\pm\frac{\alpha_c a}{H_{c2}}\left[(1-x_j)-\frac{(1-x)^2}{1+\beta_0}\right]\right.$$

$$-(1+\beta_0)(1-x_j)\ln\frac{1-x}{1-x_j}-\left[\frac{(1-x)^2}{1+\beta_0}-2\right](x-x_j)$$

$$\left.+\frac{1}{2}(x+x_j)^2-2x^2\right\} \qquad \text{(C-6)}$$

George C. Marshall Space Flight Center
National Aeronautics and Space Administration
Marshall Space Flight Center, Alabama, July 31, 1970
124-09-11-0000-80-00-000

REFERENCES

1. Livingston, J. D.: Proceedings of the 1968 Summer Study on Superconducting Devices and Accelerators, Brookhaven National Laboratory, BNL 50155 (C-55), June 10-July 19, 1968, p. 377.

2. Urban, E. W.: Cryogenics, 10, 1970, p. 62.

3. Kim, Y. B. et al.: Phys. Rev. Lett. 9, 1962, p. 306.

4. DeGennes, P. G.: Superconductivity of Metals and Alloys. Benjamin, New York, 1966.

5. Wipf, S. L., Phys. Rev. 161, 1967, p. 404.

6. Coffey, H. T.: Cryogenics 7, 1967, p. 73.

7. Wipf, S. L., and Lubell, M. S.: Phys. Lett. 16, 1965, p. 103.

8. Anderson, P. W.: Phys. Rev. Lett. 9, 1962, p. 309.

9. Kim, Y. B. et al.: Phys. Rev. 131, 1963, p. 2486.

10. Bean, C. P.: Phys. Rev. Lett. 8, 1962, p. 250.

11. London, H., Phys. Lett. 6, 1963, p. 162.

12. Kim, Y. B. et al.: Phys. Rev. 129, 1963, p. 528.

13. Friedel, J. et al.: Appl. Phys. Lett. 2, 1963, p. 119.

14. Silcox, J., and Rollins, R.: Appl. Phys. Lett. 2, 1963, p. 231.

15. Yasukochi, K. et al.: J. Phys. Soc. Japan 19, 1964, p. 1649.

16. Irie, F., and Yamafuji, K.: J. Phys. Soc. Japan 23, 1967, p. 255.

REFERENCES (Concluded)

17. Fietz, W. A. et al.: Phys. Rev. 136, 1964, p. A335.

18. Goedemoed, S. H. et al.: Physica 35, 1967, p. 273.

19. Alden, T. H., and Livingston, J. D.: J. Appl. Phys. 37, 1966, p. 3551.

20. Campbell, A. et al.: Phil. Mag. 18, 1968, p. 313.

21. Coffey, H. T.: Phys. Rev. 166, 1968, p. 447.

22. Urban, E. W.: J. Appl. Phys. 42, 1971.

23. Grigsby, D. L.: Air Force Electronic Properties Information Center Document (EPIC). DS-152, 1966.

24. Livingston, J. D., and Schadler, H. W.: Prog. Mat. Sci. 12, 1964, p. 185.

NASA-Langley, 1971 —— 26 M438

"The aeronautical and space activities of the United States shall be conducted so as to contribute . . . to the expansion of human knowledge of phenomena in the atmosphere and space. The Administration shall provide for the widest practicable and appropriate dissemination of information concerning its activities and the results thereof."

— NATIONAL AERONAUTICS AND SPACE ACT OF 1958

NASA SCIENTIFIC AND TECHNICAL PUBLICATIONS

TECHNICAL REPORTS: Scientific and technical information considered important, complete, and a lasting contribution to existing knowledge.

TECHNICAL NOTES: Information less broad in scope but nevertheless of importance as a contribution to existing knowledge.

TECHNICAL MEMORANDUMS: Information receiving limited distribution because of preliminary data, security classification, or other reasons.

CONTRACTOR REPORTS: Scientific and technical information generated under a NASA contract or grant and considered an important contribution to existing knowledge.

TECHNICAL TRANSLATIONS: Information published in a foreign language considered to merit NASA distribution in English.

SPECIAL PUBLICATIONS: Information derived from or of value to NASA activities. Publications include conference proceedings, monographs, data compilations, handbooks, sourcebooks, and special bibliographies.

TECHNOLOGY UTILIZATION PUBLICATIONS: Information on technology used by NASA that may be of particular interest in commercial and other non-aerospace applications. Publications include Tech Briefs, Technology Utilization Reports and Technology Surveys.

Details on the availability of these publications may be obtained from:

SCIENTIFIC AND TECHNICAL INFORMATION OFFICE

NATIONAL AERONAUTICS AND SPACE ADMINISTRATION

Washington, D.C. 20546